VNIVERSITAT DE VALÈNCIA Facultat de Física

MASTER'S DEGREE: ADVANCED PHYSICS

Nuclear and Particle Physics speciality

Master's Final Project

Optimisation of selection criteria of t-channel single-top-quark events at $\sqrt{s} = 13$ TeV for studies of anomalous couplings in the Wtb vertex

Pablo Martínez Agulló

September 7, 2017

Supervised by:
Susana Cabrera Urbán
Carlos Escobar Ibáñez

Abstract

The top-quark is the heaviest known fundamental particle and probing its couplings with the other fundamental particles may open a window to physics beyond the Standard Model. Single top-quark production provides a unique way to study the coupling between the top-quark, the W-boson and the b-quark, since it involves the Wtb vertex in both production and decay.

The Wtb vertex structure has been explored through the measurement of top-quark and W-boson polarisation observables using t-channel single top-quark events produced in proton-proton collisions during LHC Run I. The most recent limits on anomalous couplings in the Wtb vertex from the ATLAS and CMS experiments are reviewed.

Comprehensive studies of the t-channel selection requirements have been performed using Monte Carlo samples of signal and background events produced at $\sqrt{s} = 13$ TeV and normalised to an integrated luminosity of 36.1 pb^{-1}. Starting from events containing one isolated lepton, large missing transverse momentum and exactly two jets, one being b-tagged, stringent selection requirements are proposed to discriminate t-channel single-top events from the background contributions. These selection requirements have been designed on the basis of an statistical optimisation and regardless of kinematic properties of the top decay products that could potentially bias early measurements of top-quark polarisation in the Run II.

Acknowledgements

First and foremost I have to express my most sincere gratitude to my thesis advisor, Susana Cabrera, for her constant guidance, indefatigable coaching and for welcoming close collaboration throughout the project. Her supervision has been an enriching experience from which I have learnt a lot.

I would like to thank the ATLAS Silicon IFIC group. To Carmen García, José Enrique García and María José Costa, for being inclusive and supportive since the first day and for their advices. Also to Carlos Escobar for all his assistance and directions. I would also like to thank the PhD students Florencia Castillo, Laura Barranco and Óscar Estrada, and the freshmen Galo Gonzalvo, Jose Antonio Fernández and Marcos Martínez for their counsels.

I shall not forget the enjoyable collaboration and useful brainstorming of the t-channel polarisation analysis subgroup of ATLAS: A.Lleres (CNRS/IN2P3 Grenoble), M. de Beurs and M.Vreeswijk (NIKHEF National Institute for Subatomic Physics) and J.Mueller and J.Boudreau (University of Pittsburgh) among others.

This work has been supported by a grant founded by the IFIC Severo Ochoa formation programme 2016-2017 for master students.

Finally, I must express my very profound gratitude to my mother for providing me with unfailing support and continuous encouragement throughout my years of study. This accomplishment would not have been possible without her. Gràcies.

Contents

1 Introduction

The elementary particles, their properties and their interactions, are described by the Standard Model (SM), a quantum field theory developed in the latter half of the 20^{th} century [1]. It explains the Universe in terms of matter, made of fundamental particles called fermions (half-integer spin particles), and the fundamental forces that govern the interactions between these particles, transmitted by another set of particles called bosons (integer spin particles). It provides a unified picture of three fundamental forces: Electromagnetism, the Weak force, and the Strong force. In addition, it provides an explanation for how particle masses are created through the Higgs mechanism. The SM is very successful in giving account of most of the observed phenomena at the subatomic frontier of physics. It has been tested in many experiments in the last decades and has also predicted the existence of some particles (the quarks, the gluon, and the W, Z and Higgs bosons) before their detection.

Nevertheless, despite this success, there are still some open questions in Particle Physics that suggest that the SM is not the most complete theory. It neither describes gravity, neutrino masses, dark energy, dark matter nor matter-antimatter asymmetry (baryogenesis). Today the Universe contains mostly matter over anti-matter in its baryonic[1] component, but the SM predicts that matter and antimatter should have been created in equal amounts and so far there is no mechanism able to explain such a predominance of matter over antimatter. This baryon asymmetry is one of the greatest mysteries in physics [2] and it is understood through the so-called charge conjugation-parity (CP) violation mechanism. This discrete symmetry of nature relates the rates of particle transitions to antiparticle transitions and it is the combined operation of two individual symmetries: The charge conjugation (C), which turns a particle into its antiparticle, and the parity (P), which creates a mirror image of a physical system. If CP is conserved, the rate for a particular decay would be the same as for the related antiparticle decay. Despite the observations of violation of CP in the weak sector [3], there are not enough sources of CP violation to explain the observed matter-antimatter asymmetry in the Universe. One potential new source of CP violation may be in the top-quark sector, more specifically in the anomalous couplings of the Wtb vertex, as will be discussed in Section 2.1.

In this dissertation, the t-channel single-top-quark production at the Large Hadron Collider (LHC) (Section 3.1) has been studied using a set of Monte Carlo (MC) simulated event samples produced for the t-channel signal and for all the SM processes, all of them generated with a centre-of-mass energy of 13 TeV and normalised to an integrated luminosity of 36.1 pb^{-1}. This luminosity was recorded by the ATLAS experiment in 2015 and 2016. The main goal of this work is to perform a statistical optimisation of the criteria to select a signal sample enriched in t-channel single-top-quark events that will be used in the measurements of polarisation observables by the ATLAS experiment during Run II. This requires the establishment of a set of kinematic cuts that optimise the event selection, i.e. boundaries that enhance the statistical significance and the signal to background ratio (S/B). This work is motivated by the fact that, when produced in

[1] Nearly all matter that may be encountered or experienced in everyday life is baryonic matter (which includes atoms of any kind).

t-channel, the top quark has a large degree of polarisation in the direction of the light-flavour quark momentum [4], which allows us to measure asymmetries which are related to CP violation in the Wtb-vertex Lagrangian (Section 2).

The theoretical framework regarding the Wtb vertex and the polarisation of the top quark is detailed in Section 2. The ATLAS experiment, in which this master thesis is contextualised is introduced in Section 3. Section 4 describews the set of MC samples used as well as the preselection requirements. In Section 5 is explained the methodology followed in order to define the optimised selection and the final results. Finally, the conclusions are summarized in Section 6.

2 Theoretical framework: The Wtb vertex and top quark polarisation

2.1 The Wtb vertex structure in t-channel single-top-quark production and decay

The top quark is the heaviest elementary particle discovered so far, with a mass of $m_{top} = 172.44 \pm 0.13(\text{stat}) \pm 0.47(\text{syst})$ GeV [5], followed by the Higgs boson, with $m_H = 125.09 \pm 0.21(\text{stat.}) \pm 0.11(\text{syst.})$ GeV [6]. In the context of the SM, the top quark is the isospin[2] partner of the b-quark, which is 35 times lighter [7]. Due to its large mass, measurements of phenomena involving the top-quark physics are crucial to our understanding of the electroweak sector in the SM or beyond the SM (BSM) theories.

In 1973 M. Kobayashi and T. Maskawa postulated the top quark in order to explain the CP violations in kaon decay [8]. It was later discovered in 1995 by the CDF [9] and DØ [10] experiments at Fermilab. The Nobel Prize in Physics 2008 [11] was divided in two halves, one half was conceded to Y. Nambu "for the discovery of the mechanism of spontaneous broken symmetry in subatomic physics" and the other half was shared among M. Kobayashi and T. Maskawa "for the discovery of the origin of the broken symmetry which predicts the existence of at least three families of quarks in nature".

The top quark decays to a W boson and a down-type quark via flavour changing electroweak processes. The branching ratios (BR) of its decays are related to the Cabibbo-Kobayashi-Maskawa (CKM) matrix elements:

$$\frac{BR(t \to Wb)}{BR(t \to Wq)} = \frac{|V_{tb}|^2}{\sum |V_{tq}|^2} = |V_{tb}|^2 \approx 1 \tag{1}$$

where q stands for the three possible quarks to which top quark can decay: d, s and b. Expression 1 means that the top quark decay happens almost always to a b-quark and a W boson.

[2]Particles that are identically affected by strong interactions but have different charges can be treated as being different states of the same particle with isospin values related to the number of charge states.

As a consequence of the huge mass of the top quark, its life time is extremely short, $\mathcal{O}(10^{-25}$ s). It is shorter than the time scale of quantum chromodynamics (QCD), $\mathcal{O}(10^{-24}$ s), allowing this quark to be studied as a free quark. Therefore, the top quark decays before hadronising. Moreover, since its lifetime is also shorter than the depolarisation timescale, $\mathcal{O}(10^{-21}$ s) [12], and the W boson is produced on-shell in the top-quark decay, the top-quark spin information is directly transferred to its decay products. Thus, we can measure its polarisation from its decay products.

The top quark decay is classified in different channels depending on the decay of the W boson. The W boson can decay either leptonically into a lepton and its corresponding antineutrino or hadronically into two quarks ($u\bar{d}$ or $c\bar{s}$). The relative branching ratio:

$$\frac{BR(W \to q\bar{q})}{BR(W \to l\bar{\nu})} = \frac{BR(W \to c\bar{s}, u\bar{d}) \times colour}{BR(W \to e, \mu, \tau)} = 6/3 \tag{2}$$

In the t- and s-channels, where only one W boson is produced, it is possible to classify two samples: the hadronic and the leptonic one. The leptonic sample includes the leptonic decays of the W boson into electrons, muons or leptonic taus decays, plus their corresponding antineutrinos. On the other hand, the hadronic sample comprises the hadronic W-boson decays and the hadronic-tau decays[3]. The scope of the presented analysis is the study of the t-channel single-top-quark events with the top quark decaying into leptonic W bosons, with an electron in the final state.

In hadron colliders there are two production mechanisms of top quark: top-quark pairs ($t\bar{t}$) and single-top quarks. Single-top quarks are produced, at leading order (LO) in QCD perturbation theory, by three different electroweak subprocesses: the exchange of a virtual W boson in the t-channel or the s-channel, or the case with an on-shell W boson [13] (Figure 1). As can be seen in Table 1, the t-channel dominates the single-top production.For the $\sqrt{s} = 13$ TeV data, the total cross-sections for both top quark and top antiquark production are measured to be $\sigma(tq) = 156 \pm 5$(stat.) ± 27(syst.) ± 3(lumi.) pb and $\sigma(\bar{t}q) = 32.9 \pm 4$(stat.) ± 18(syst.) ± 2(lumi.) pb, respectively [14] [15]. The cross-section ratio of top-quark to top-antiquark production is, therefore, $R_t = \frac{\sigma(tq)}{\sigma(\bar{t}q)} = 1.72 \pm 0.09$(stat.) ± 0.18(syst.).

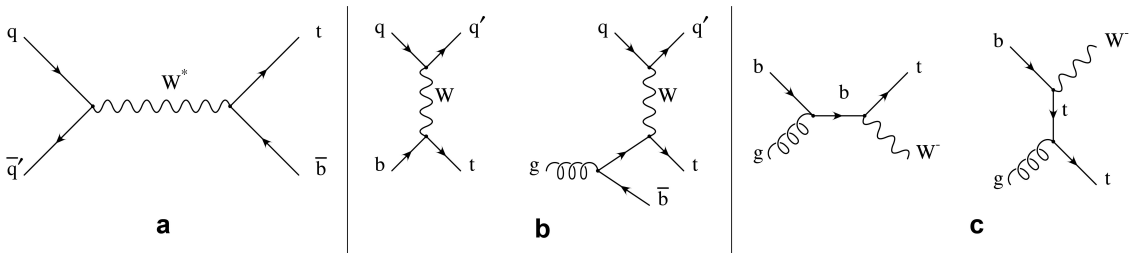

Figure 1: Feynman diagrams for single top quarks production in pp collisions: a) s-channel b) t-channel c) Wt associated decay.

Top-quark production at LHC is dominated by $t\bar{t}$ via flavour-conserving strong interactions, but single-top quark can be produced through charged-current electroweak

[3]The lepton τ is the only lepton that can decay into hadrons, occurring 64.79% times. The predominant hadronic decay is into a charged pion, a neutral pion, and a tau neutrino. The non-hadronic decays are into an electron or a muon, occurring 17.82% and 17.39% of times respectively [7], plus their corresponding neutrinos.

$\sqrt{s}$ (TeV)	σ_{t-chan} (pb)	$\sigma_{Wt-chan}$ (pb)	$\sigma_{s-channel}$ (pb)
8	$87.76\pm^{3.44}_{1.91}$ [16]	22.37 ± 1.52 [17]	5.61 ± 0.22 [18]
13	$216.99\pm^{9.04}_{7.71}$ [19] [20]	71.7 ± 3.8 [17]	$10.32\pm^{0.40}_{0.36}$ [19] [20]

Table 1: Theoretical inclusive cross-section predictions of the single-top-quark production processes at LHC with $\sqrt{s} = 8$ and 13 TeV.

processes. The dominant process, t-channel, has two representations at LO. In Figure 1-b, q represents a light-flavour $\bar{d}$ or u quark, and q' represents a light-flavour $\bar{u}$ or d quark, called spectator quark. On the left-hand side of the t-channel diagrams, the initial b-quark comes from the sea, this is what is named a $2 \to 2$ process. On its right-hand side, the b-quark comes from the splitting of a gluon into a pair $b\bar{b}$ in the so called $2 \to 3$ process.

Probes of new physics phenomena related to the production or decay of the top can be parametrised with a series of effective couplings at each vertex. Both production and decay occur through the Wtb vertex in t-channel single-top production in a way that the same formalism can be used to describe both cases. In effective operator formalism, the Lagrangian for the Wtb vertex can be written in full generality as [21]:

$$\mathcal{L}_{Wtb} = -\frac{g}{\sqrt{2}}\bar{b}\gamma^{\mu}(V_L P_L + V_R P_R)tW^-_{\mu} - \frac{g}{\sqrt{2}}\bar{b}\frac{i\sigma^{\mu\nu}q_{\nu}}{m_W}(g_L P_L + g_R P_R)tW^-_{\mu} + h.c. \qquad (3)$$

In order to preserve unitarity, this Lagrangian is assumed to be Hermitian. The operators P_L and P_R are defined as the left- and right-handed operators representing the different treatment of left-handed and right-handed fermions in the weak interaction. All complex phases in our effective Lagrangian are CP violating [22]. In the context of SM, equation (3) has, at tree level, $V_L = V_{tb} \approx 1$ and $V_R = g_L = g_R = 0$, deviations from these values would indicate new physics. By measuring certain observables, we can quantify this any such deviations. We are particularly interested by possible existence of non-zero anomalous couplings V_R, g_L and g_R.

Hereafter, we have reviewed the limits at the 95% confidence level set by ATLAS and CMS using Run I data:

- Reference [13]: ATLAS has set limits on $\mathrm{Im}\{g_R\}$ assuming $V_L = 1$ and that all anomalous couplings other than $\mathrm{Im}\{g_R\}$ vanish using measurements of angular asymmetries of polarisation observables obtained from t-channel single-top-quark events produced at $\sqrt{s} = 8$ TeV and with a data sample with an integrated luminosity (L_{int}) of 20.2 fb^{-1}.
  - $\mathrm{Im}\{g_R\} \in [-0.18, 0.06]$
- Reference [23]: ATLAS set limits on anomalous couplings V_R, g_L and g_R from the measurement of the W-boson helicity fractions F_R, F_L and F_0 performed at $\sqrt{s} = 8$ TeV and $L_{\mathrm{int}} = 20.2$ fb^{-1} and using dileptonic and single lepton $t\bar{t}$ events. This is performed by exploiting the dependence of these fractions on the couplings, assuming $V_L = 1$ and taking only one of the rest of couplings non-zero at a time.
  - $\mathrm{Re}\{g_R\} \in [-0.02, 0.06], [0.74, 0.78]$

  - $\mathrm{Re}\{g_L\} \in [-0.14, 0.11]$
  - $\mathrm{Re}\{V_R\} \in [-0.24, 0.31]$

- Reference [24]: ATLAS has placed limits simultaneously on possible complex values of ratios of anomalous couplings with no assumptions on values of the other anomalous couplings using the measurement of the normalised triple-differential angular decay rate of the top quark in t-channel single-top-quark events produced at $\sqrt{s} = 8$ TeV and with a data sample with an integrated luminosity of 20.2 fb^{-1}.

  - $|V_R/V_L| < 0.37$
  - $|g_L/V_L| < 0.29$
  - $\mathrm{Re}\{g_R/V_L\} \in [-0.12, 0.17]$
  - $\mathrm{Im}\{g_R/V_L\} \in [-0.07, 0.06]$

- Reference [25]: CMS has also placed limits using t-channel single-top events produced at $\sqrt{s} = 7$ and 8 TeV, and with data samples with $L_{\mathrm{int}} = 5.0$ and 19.7 fb^{-1} respectively. The combined limits in three-dimensional scenarios on possible Wtb anomalous couplings are:

  - $V_L > 0.98$
  - $|V_R| < 0.16$
  - $|g_L| < 0.057$
  - $g_R \in [-0.049, 0.048]$

2.2 Top-quark polarisation and W-boson spin observables

In this section we describe the theoretical framework considered in the studies performed in this master thesis, where some of the angular distributions defined in this framework will be considered when designing the selection criteria of an enriched t-channel sample at 13 TeV to be used in future measurements of t-channel polarisation studies in the LHC Run I.

When produced at hadron colliders, single-top quarks are the only source of highly polarised top quarks. Specifically, in the t-channel, the top quark is produced with a large degree of polarisation in the direction of the spectator quark momentum [26]. As the top quark is extremely unstable, its polarisation must be inferred from the analysis of the angular distributions of the decay products, W and b, in the top-quark reference frame. The angular distribution of the charged lepton ($l = e$, μ) from $t \to Wb \to l\nu b$ is usually used, because it is the most sensitive to the top-quark polarisation [27].

Defining the reference system with axes (x, y, z) in the top-quark rest frame, the state of an ensemble of polarised top quarks can be described by a density matrix

$$\rho = \frac{1}{2} = \begin{pmatrix} 1 + P_z & P_x - iP_y \\ P_x + iP_y & 1 - P_z \end{pmatrix} \tag{4}$$

where the polarisation in an axis is twice the expected value of the spin in that axis: $P_i = 2\langle S_i \rangle$, being $i = x, y, z$. The top-quark spin direction is defined in the direction of the spectator quark momentum in the rest frame of the top quark. The three-dimensional vector $\overrightarrow{P}$ satisfies generally that $|\overrightarrow{P}| \leq 1$, and $|\overrightarrow{P}| = 1$ if and only if the quarks are produced as a pure spin state [21]. The three orthogonal axis can be taken as:

- $\hat{z}$-axis: The direction of the spectator quark three-momentum, $\overrightarrow{p_j}$.

$$\hat{z} = \frac{\overrightarrow{p_j}}{|\overrightarrow{p_j}|} \tag{5}$$

- $\hat{y}$-axis: Orthogonal to $\overrightarrow{p_j}$ and the initial quark three-momentum, $\overrightarrow{p_q}$.

$$\hat{y} = \frac{\overrightarrow{p_j} \times \overrightarrow{p_q}}{|\overrightarrow{p_j} \times \overrightarrow{p_q}|} \tag{6}$$

- $\hat{x}$-axis: Orthogonal to $\hat{z}$ and $\hat{y}$ and requiring that the coordinate system is right handed.

$$\hat{x} = \hat{y} \times \hat{z} \tag{7}$$

Both vectors, $\overrightarrow{p_j}$ and $\overrightarrow{p_q}$ are measured in the top quark rest frame. The direction of $\hat{z}$ is called *longitudinal*, $\hat{x}$ direction *tranverse* and $\hat{y}$ is the *normal*. It has to be noticed that the momentum direction of the initial quark in the t-channel cannot be determined unambiguously in hadronic collisions.

It is necessary to chose between the two proton beam directions to define the direction of the initial quark in $gq \to q't\bar{b}$ so that we can construct the (x, y, z) reference system. To do this, one can use the momentum of the spectator quark in the laboratory frame, which most times follows that of the initial quark (this choice gives the correct answer 97% times for $ug \to dt\bar{b}$ and 98% times for $dg \to ub\bar{t}$, the main channel for single top and top antiquark production).

For top quark and antiquark we have the following SM polarisations [21]:

$$\overrightarrow{P} \approx (0, 0, 0.90) \qquad (t)$$
$$\overrightarrow{P} \approx (-0.14, 0, -0.86) \qquad (\bar{t})$$

Those calculus are computed for the $2 \to 3$ process $qg \to q't\bar{b}$ with the generator PROTOS [28], using CTEQ6L1 [29] parton distribution functions. The longitudinal agrees with the next-to-leading-order (NLO) calculatios [30]; $P_z = 0.91$ for quarks and $P_z = -0.86$ for antiquarks. Aditionally, several kinematic distributions are similar [31]. Notice that, in the SM, P_x is not zero for antiquarks because the spectator quark is not the d quarks in the leading production process, $dg \to ut\bar{b}$ [4]. The presence of new physics in the t-channel single-top productions changes completely this SM predictions [22].

The variations of P_i when a single anomalous coupling from the Lagrangian (3) is non-zero is shown in Figure 2. The V_L is set to 0 from now on and the range for the

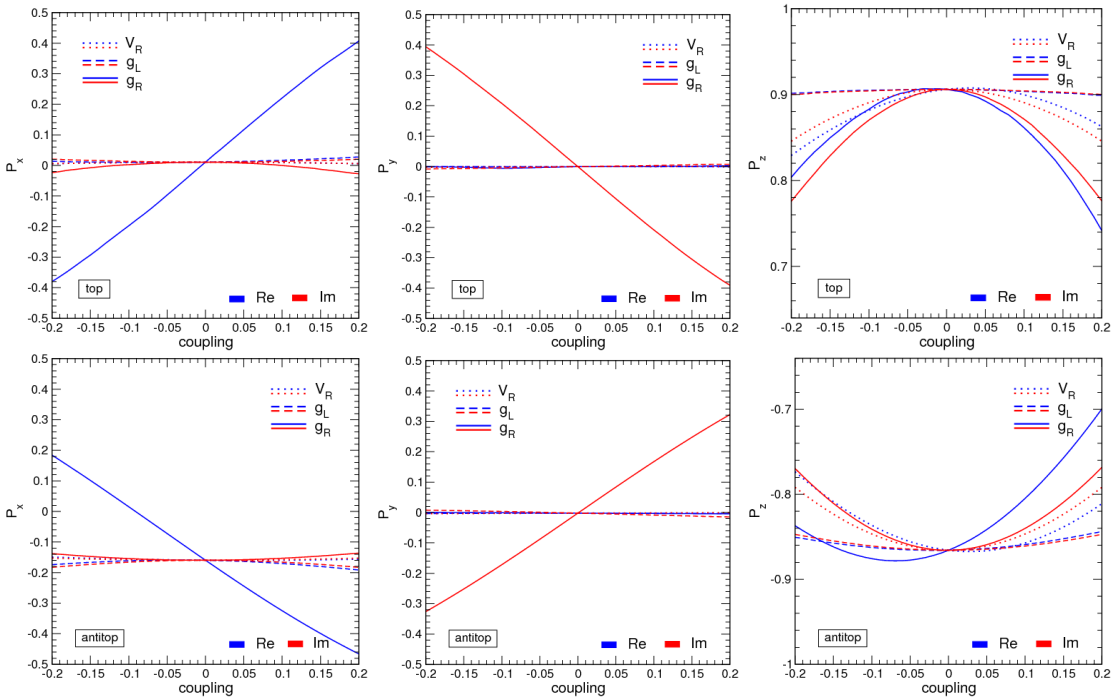

Figure 2: Single top quark (upper row) and antiquark (lower row) polarisation in the axes defined in the equations (5), (6) and 7 as a function of the different coupling constants. The V_L is set to zero [22].

anomalous couplings is, according to the order of the current direct limit, $[-0.2, 0.2]$. The dependence of the top quark polarisation on anomalous couplings can be extracted from a fit and the resulting expressions are for top quarks [22]:

$$P_x = (-0.13|V_R|^2 + 0.25|g_L|^2 - 0.90|g_R|^2 + 2.14Re\{V_L^* g_R\} - 1.53Re\{V_R^* g_L\})/f_t$$
$$P_y = (-2.12Im\{V_L^* g_R\} - 1.54Im\{V_R^* g_L\})/f_t$$
$$P_z = (0.90 - 0.76|V_R|^2 - 1.15|g_L|^2 - 1.50|g_R|^2 - 0.60Re\{V_L^* g_R\} + 0.36Re\{V_R^* g_L\})/f_t$$

and for the top antiquarks [22]:

$$P_x = (-0.14|V_R|^2 - 0.96|g_L|^2 + 0.34|g_R|^2 - 1.71Re\{V_L^* g_R\} + 2.31Re\{V_R^* g_L\})/f_{\bar{t}}$$
$$P_y = (1.72Im\{V_L^* g_R\}2.30Im\{V_R^* g_L\})/f_{\bar{t}}$$
$$P_z = (-0.86 + 0.99|V_R|^2 - 1.56|g_L|^2 + 1.20|g_R|^2 + 0.42Re\{V_L^* g_R\} - 0.67Re\{V_R^* g_L\})/f_{\bar{t}}$$

Where f_t and $f_{\bar{t}}$ are correction factors for the total corss sections with anomalous couplings [28]:

$$f_t = 1 + 0.90|V_R|^2 + 1.47|g_L|^2 + 2.31|g_R|^2 - 0.11Re\{V_L^* V_R\} - 0.53Re\{V_L^* g_R\}$$
$$f_{\bar{t}} = 1 + 1.09|V_R|^2 + 2.36|g_L|^2 + 1.58|g_R|^2 - 0.12Re\{V_L^* V_R\} - 0.56Re\{V_L^* g_R\}$$

The reason for appearance of imaginary parts of coupling products in P_y and not P_x nor P_z, can be understood from the $2 \to 2$ approximation to the t-channel. Since the differential cross section is proportional to the square of the modulus of the matrix element, and there are no absorptive parts, those elements can only arise from the

traces of Dirac matrices $Tr\{\gamma^5\gamma^\mu\gamma^\nu\gamma^\rho\gamma^\sigma\} = -4i\epsilon^{\mu\nu\rho\sigma}$ contracted with four different 4-vectors, being $\epsilon^{\mu\nu\rho\sigma}$ the totally antisymmetric tensor. There are only three independent 4-momenta in the $2 \to 2$ processes. Therefore, the 4-vector in a non-zero contraction must be the top-spin vector, $\overrightarrow{s_t}$. The Lorentz-invariant contraction $\epsilon_{\mu\nu\rho\sigma}p_q^\mu p_j^\nu p_t^\rho s_t^\sigma$ is proportional to $(\overrightarrow{p_q} \times \overrightarrow{p_j}) \cdot \overrightarrow{s_t}$, in the top quark rest frame. The triple product vanishes for $\overrightarrow{s_t}$ in the $\hat{x}$ and $\hat{z}$ but not for the $\hat{y}$ one. This argument is not very affected by the extra b quark in the $2 \to 3$ process because it is mostly collinear to the beam direction.

A study of top-quark physics contributes to the understanding of the origin of the electro-weak symmetry breaking in the SM and its extensions. As mentioned before, the top-quark polarisation is determined from angular distributions of the decay products reconstructed in the top-quark rest frame, while the W-boson spin observables are determined from angular distributions of the charged lepton reconstructed in the W-boson rest frame. In the top-quark rest frame, the angular distribution of any decay product X of the top quark is given by:

$$\frac{1}{\Gamma}\frac{d\Gamma}{d(\cos\theta_X)} = \frac{1}{2}(1 + P\alpha_X \cos\theta_X) \tag{8}$$

where θ_X is the angle between the direction of motion of the decay product in top's rest frame and the top-quark spin axis. α_X is a constant called *spin analysing power* of X, P is the top quark degree of polarisation with $0 \leq P \leq 1$ and Γ is the total decay width. This P is the one described previously with the components $P_i = Px$, P_y, P_z as defined in equations (7) (6) (5).

That is, α_X relates the top-quark spin to the angular distribution of the decay product X, and it is the fraction of polarisation transferred to the decay products. The most sensitive spin analyser is the charged lepton; at NLO precision in QCD its spin analysing power is $\alpha_{l^\pm} = \pm 0.998$ [32]. From [33] can be calculated the product of the top momentum and the spin analysing power of the lepton which is $P \cdot \alpha_\mu = 0.58 \pm 22$ for the top and $P \cdot \alpha_\mu = 0.42 \pm 28$ for the anti-top. The combination of both is $P \cdot \alpha_\mu = 0.52 \pm 22$.

From the spin density matrix in Equation (4), W-boson helicity components 0 and ± 1 resulting from the decay of polarised top-quarks, can be parameterised in terms of expectation values of six independent spin observables [13] $\langle S_{1,2,3}\rangle$, $\langle A_{1,2}\rangle$ and $\langle T_0\rangle$. The polar and azimuthal angles of the charged lepton in the W-boson rest frame are denoted by θ_l^* and ϕ_l^*; from now on, the variables with the star (*) are in the W-boson rest frame. The fully differential decay width of W can be written as:

$$\begin{aligned}\frac{1}{\Gamma}\frac{d\Gamma}{d(\cos\theta_l^*)d\phi_l^*} =& \frac{3}{8\pi}\Big\{\frac{3}{2} + \frac{1}{\sqrt{6}}\langle T_0\rangle(3\cos^2\theta_l^* - 1) + \langle S_3\rangle\cos\theta_l^* \\ &+ \langle S_1\rangle\cos\phi_l^*\sin\theta_l^* + \langle S_2\rangle\sin\phi_l^*\sin\theta_l^* \\ &- \langle A_1\rangle\cos\phi_l^*\sin 2\theta_l^* - \langle A_2\rangle\sin\phi_l^*\sin 2\theta_l^*\Big\}\end{aligned} \tag{9}$$

In this formalism the W-boson spin axis is taken along the direction of the W-boson momentum in the top-quark rest frame, or equivalently along the direction opposite to the b-quark momentum in the W-boson rest frame. In Figure 3 can be seen the coordinate system used and the various angles defined for the charged lepton in the W

rest frame. Here, the axis are defined as follows: $\hat{z}$ is the W-boson momentum direction in the top-quark rest frame; the direction of top's spin, $\hat{s}_t$, taken along the spectator quark momentum in top quark rest frame defines the $\hat{x}$-$\hat{z}$ plane. The momentum of the charged lepton is $\overrightarrow{p_l}$ in the W rest frame. The normal and transverse axes are defined relatively to $\overrightarrow{q}$ and $\hat{s}_t$ according to $\overrightarrow{N} = \hat{s}_t \times \overrightarrow{q}$ and $\overrightarrow{T} = \overrightarrow{q} \times \overrightarrow{N}$; they are along the $-\hat{y}$ and $\hat{x}$ axes of the coordinate system, respectively. The azimuthal angles of the charged lepton in the W-boson rest frame (ϕ^*_N,$\phi^*_T \equiv \phi^*_l$) are defined relatively to the $\overrightarrow{N}$ and $\overrightarrow{T}$ axes while θ^N_l and θ^T_l, which are not showm in the Figure 3, are the relative angles between the $\overrightarrow{N}$ and the $\overrightarrow{T}$ and axes respectively.

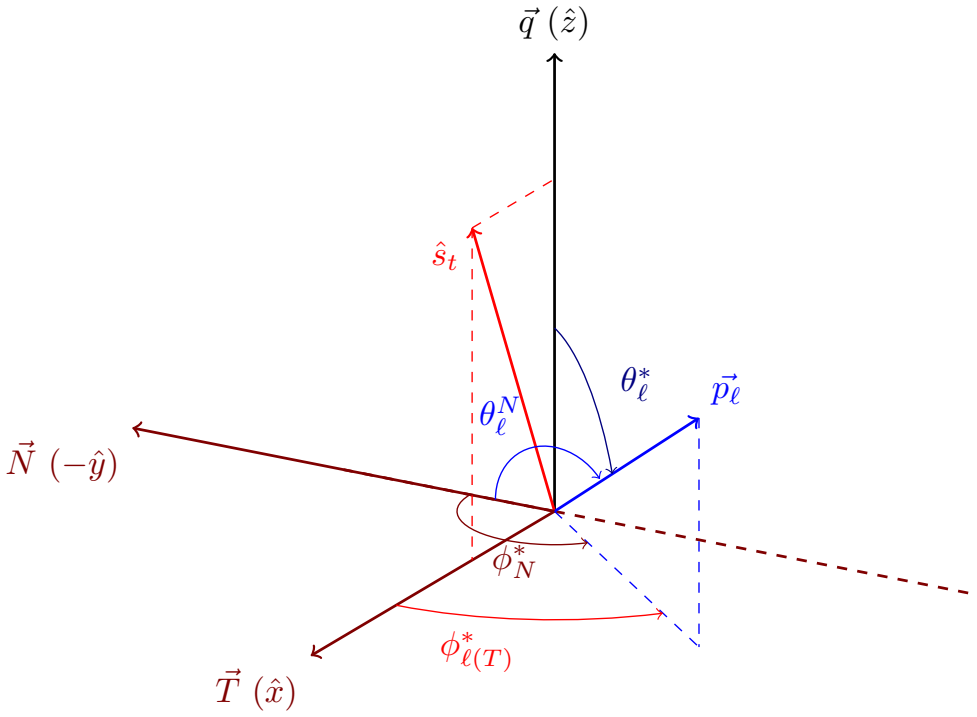

Figure 3: Coordinate system and angles used to define the W-boson spin observables and their related angular asymmetries in the decay of polarised top quarks.

There is an integral over all the possible direction of the top-quark spin relative to the W-boson spin axis implied by the angular distribution of equation (9). The polarisation of the top quark is propagated to the spin observables $\langle S_{1,2} \rangle$ and $\langle A_{1,2} \rangle$, which are proportional to P. The other spin observables $\langle S_3 \rangle$ and $\langle T_0 \rangle$ are not depending on P and are related to the W-boson helicity fractions: F_R, F_L and F_0 [34].

Using the SM predictions of the helicity fractions at next-to-next-leading-order (NNLO) in QCD, assuming a top mass of 172.5 GeV and a b-quark mass of 4.8 GeV [35], it is found that $\langle S_3 \rangle = -0.31 \pm 0.01$ and $\langle T_0 \rangle = -0.43 \pm 0.01$. The polarisation-dependent spin observables can be obtained combining the predicted degrees of polarisation ($P_t = 0.91$ and $P_{\bar{t}} = -0.86$) with the t-channel single-top cross sections ($\sigma_t = 54.9$ pb and $\sigma_{\bar{t}} = 29.7$ pb) calculated at NLO in QCD. Then, the SM predictions calculated at LO in QCD for $\langle S_{1,2} \rangle$ and $\langle A_{1,2} \rangle$ are: $\langle S_1 \rangle = 0.46 \pm 0.01$, $\langle A_1 \rangle = 0.23 \pm 0.01$ and $\langle S_2 \rangle = \langle A_2 \rangle = 0.00 \pm 0.01$ [13]. If the measured values of $\langle S_2 \rangle$ and $\langle A_2 \rangle$ spin observables were different of zero, it would imply the presence of an imaginary coupling in the Wtb vertex (eq. (3))

Asymmetry	Angular Observable	polarisation observable	SM prediction (± 0.01)
A_{FB}^{l}	$\cos\theta_l$	$\frac{1}{2}\alpha_l P$	0.45
A_{FB}^{tW}	$\cos\theta_W \cos\theta_l^*$	$\frac{3}{8}P(F_R + F_L)$	0.10
A_{FB}	$\cos\theta_l^*$	$\frac{3}{4}\langle S_3\rangle = \frac{3}{4}(F_R - F_L)$	-0.23
A_{EC}	$\cos\theta_l^*$	$\frac{3}{8}\sqrt{\frac{3}{2}}\langle T_0\rangle = \frac{3}{16}(1 - F_0)$	-0.20
A_{FB}^{T}	$\cos\theta_l^T$	$\frac{3}{4}\langle S_1\rangle$	0.34
A_{FB}^{N}	$\cos\theta_l^N$	$-\frac{3}{4}\langle S_2\rangle$	0
$A_{FB}^{T,\phi}$	$\cos\theta_l^* \cos\phi_T^*$	$-\frac{2}{\pi}\langle A_1\rangle$	-0.14
$A_{FB}^{N,\phi}$	$\cos\theta_l^* \cos\phi_N^*$	$\frac{2}{\pi}\langle A_2\rangle$	0

Table 2: Asymmetries with their associated angular observables and their relation to the top-quark polarisation and W-boson spin observables.

since those observables are only sensitive to $\mathrm{Im}\{g_R\}$ [13]. The observable $\langle S_2\rangle$ is twice ar sensitive as $\langle A_2\rangle$ to $\mathrm{Im}\{g_R\}$, which makes it more suitable for determining this coupling. The other four W-boson spin observables are mainly sensitive to $\mathrm{Re}\{g_R\}$, having a poor sensitivity to $\mathrm{Im}\{g_R\}$.

The W-boson spin observables and top-quark polarisation can be extracted from asymmetries derived by integrating the angular distributions expressed in equations (8) and (9). These asymmetries are based on single or combined angular observables. A list of the asymmetries, their associated angular observables, their relation to the polarisation observables and their values predicted by the SM can be found on Table 2.

The forward-backward (FB) asymmetry, in which most polarisation observables used here are based on, is defined as a function of a given angular observable $\cos\theta$ according to

$$A_{FB} = \frac{N(\cos\theta > 0) - N(\cos\theta < 0)}{N(\cos\theta > 0) + N(\cos\theta < 0)} \tag{10}$$

where N is the number of events. For the W, the other used asymmetry is the so called edge-central (EC), which is similarly defined

$$A_{EC} = \frac{N(\cos\theta > \frac{1}{2}) - N(\cos\theta < \frac{1}{2})}{N(\cos\theta > \frac{1}{2}) + N(\cos\theta < \frac{1}{2})} \tag{11}$$

The asymmetry A_{FB}^{l} allows us to determine the product $\alpha_l P$ from the angular distribution $\cos\theta_l$, being θ_l the angle between the lepton momentum in the top quark rest frame and the top-quark spin axis. From the A_{FB}^{tW} is possible to obtain P; this asymmetry is defined with respect to the combined angular observable $\cos\theta_W \cos\theta_l^*$ (see Table 2), where θ_W is the angle between the W-boson momentum in the top-quark rest frame and the top-quark spin axis. The W-boson spin observables $\langle S_3\rangle$ and $\langle T_0\rangle$ are derived from the forward-backward asymmetry A_{FB} and from the edge-central asymmetry A_{EC} of the $\cos\theta_l^*$ angular distribution, respectively. The $\langle S_1\rangle$ and $\langle S_2\rangle$ are determine from A_{FB}^{T} A_{FB}^{N} in the angular observables $\cos\theta_l^T$ and $\cos\theta_l^N$, respectively. The spin observables $\langle A_1\rangle$ and

$\langle A_2 \rangle$ are extracted from $A_{FB}^{T,\phi}$ and $A_{FB}^{N,\phi}$. This is based on the W-boson helicity, $\cos\theta_l^*$, multiplied per the cosine of ϕ_T^* and ϕ_N^* defined with respect to $\overrightarrow{T}$ and $\overrightarrow{N}$, respectively.

The asymmetry A_{FB}^N is very sensible to the coupling g_R, therefore it can be used to extract limits on $\mathrm{Im}\{g_r\}$. Considering small values of $\mathrm{Im}\{g_r\}$ and taking $V_L = 1$ and $v_R = g_L = 0$, a linear dependence of the form $A_{FB}^N = 0.64 \cdot P \cdot \mathrm{Im}\{g_r\}$ is obtained [21]. As A_{FB}^N depends on P, the measured value of the A_{FB}^l asymmetry is required to constrain P for the limit computation.

3 The ATLAS experiment

3.1 CERN and LHC

After Second World War, Europe was tore apart and its science was no longer world-class. As a reaction to this, French physicist Louis de Broglie put forward the first official proposal for the creation of a European laboratory at the European Cultural Conference, which opened in Lausanne on 9 December 1949. In 1952, with the mandate of establishing a world-class fundamental physics research organization in the continent, a provisional body was founded in 1952. On the 29^{th} September 1954, the *Conseil Européen pour la Recherche Nucléaire* (European Council for Nuclear Research, CERN) was founded by 12 countries. Despite the early change of the name to *European Organization for Nuclear Research*, the acronym remains unchanged until nowadays. Based in Geneva, currently it is the world largest particle physics center and it includes 22 member states.

Several scientific achievements have been made through CERN experiments, for instance: the discovery of neutral currents [36], the W and Z bosons [37], the determination of the number of light neutrino families [38], the direct discovery of CP violation [39] or Higgs boson discovery [40].

Aproved by CERN Council in 1994 and started for first time in 2008, the Large Hadron collider (LHC) is the world's newest and most powerful tool for Particle Physics research [41]. The LHC is a two-ring super accelerator proton-proton collider built along the 27 km of LEP, the electron-positron accelerator used in CERN from 1989 to 2000 [42]. The aim of the hadronic collider was to discover the Higgs boson, which was achieved in 2012, as well as to study rare events. It is designed to collide two beams of hadrons, mainly protons, with a centre-of-mass energy of the collision of $\sqrt{s} = 14$ TeV and an instantanius luminosity of 10^{34} cm^{-2}s^{-1}. Apart from protons, it can also collide heavy (Pb) ions with an energy of 2.8 TeV per nucleon and a peak luminosity of 10^{27} cm^{-2}s^{-1} [43]. An scheme of LHC and its injection system can be seen in Figure 4.

The proton bunches are produced ionizing hydrogen atoms and then sent through a series of preaccelerators that boost the hadrons until they have an energy[4] of 450 GeV. At this point, two sets of proton beams are injected in the LHC pipes in opposite directions. The beams keep aligned and stable thanks to the superconducting dipoles and

[4]Minimum energy at which the LHC can maintain a stable beam.

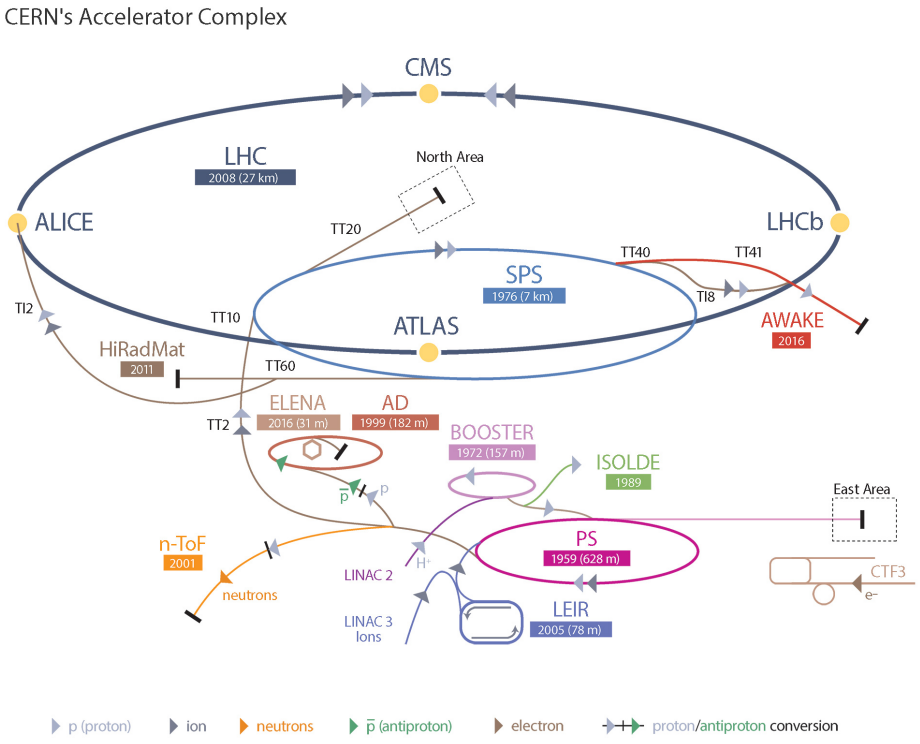

Figure 4: Scheme of CERN accelerator complex.

quadrupole magnets. Once the protons are in the main rings, their energy is raised by increasing the intensity of the magnetic field from 0.54 T to 8.3 T. If the energy is maintained, the beams are declared stable and the different experiments start the data taking. The beams collide at the points where the detectors are located during periods of time of 24 h or less. The beams stop circulating through the rings when they lose stability or the losses of protons due to the collisions make the quality of the beams insufficient. At this stage the beam is directed out of the accelerator and the magnets ramped down to 0.54 T.

There are four main experiments in the LHC (ATLAS, CMS, LHCb and ALICE) and two smaller (TOTEM and LHCf). All of them sit underground in huge caverns on the LHC ring. The biggest of these are ATLAS and CMS [44], which use general-purpose detectors to investigate the largest range of physics possible. CMS and ATLAS detectors are independently designed to ensure a real cross-checking of new discoveries. ALICE, LHCb, TOTEM and LHCf have detectors specialized on specific phenomena. ALICE [45] is dedicated to heavy ion (Pb-Pb) experiments, LHCb [46] searches for b-physics, TOTEM [47] does for protons from elastic scattering at small angles and LHCf [48] does for neutral pions produced in the forward direction. There is a minor experiment hold at LHC that worth to be mentioned, MoEDAL, which uses detectors deployed near LHCb to search for the magnetic monopole [49]. The simulated events used for this project are generated for the ATLAS detector, explained in section 3.2.

	Design	2010	2011	2012	2015	June 2016
Beam energy (TeV)	7.0	3.5	3.5	4.0	6.5	6.5
Protons/Bunch ($\times 10^{11}$)	1.15	1.0	1.3	1.5	1.1	1.1
Maximum number of bunches	2808	368	1380	1380	2244	2076
Bunch spacing (ns)	25	150	50	50	25	25
Maximum peak luminosity ($\times 10^{11}$ cm^{-2}s^{-1})	1.0	0.021	0.35	0.77	0.51	1.01
Total integrated luminosity (fb^{-1})		0.048	5.5	22.8	4.2	8.1

Table 3: Parameters of LHC during Run I and Run II (unitil June 2016) [51].

Performance

An important feature of LHC operation is the luminosity, which measures the number of collisions produced by the accelerator. The instantaneous luminosity ($\mathcal{L}_{ins}$) provides the rate of events given the cross section (σ_{event}) of the event under study:

$$\frac{dN_{event}}{dt} = \mathcal{L}_{ins} \cdot \sigma_{event}$$

If two bunches containing n_1 and n_2 particles collide head-on with the frequency of bunch crossing f , a basic expression for the luminosity is [50]:

$$\mathcal{L}_{ins} = f \cdot \frac{n_1 n_2 n_b}{4\pi\sigma_x\sigma_y} \cdot F(\theta_c, \sigma_x, \sigma_z)$$

At the LHC, f has a value of $f = 11245.5$ Hz, calculated from its length (27 km) and assuming that the particles there travel at the speed of light. The maximum number of proton bunches in the machine with 25 ns slots is $n_b = 2808$; the theoretical maximum of 3564 bunches cannot be reached due to space needed between bunch trains and for the beam dump kicker magnets. The $n_1 \approx n_2 \approx 1.15 \times 10^{11}$. $\sigma_x \approx \sigma_y \approx 12, ..., 50$ μm are the rms transverse beam sizes in the horizontal and vertical directions, this characterize the beam optics. Finally, the factor $F(\theta_c, \sigma_x, \sigma_z)$ accounts for luminosity reduction due to the beam crossing angle θ_c. As can be seen, $\mathcal{L}_{ins}$ only depends on the machine and its beam parameters [7].

During the first proton run, that took place between 2010 and 2013, the experiment was carried out at 3.5 TeV with a bunch spacing of 50 ns instead of the 25 ns. This implied fewer bunches with larger intensity and hence a high peak luminosity but larger pileup than nominal. Run I resulted in about 30 fb^{-1} of proton data (which was used for the Higgs boson discovery). Run I was followed by a long shutdown (LS1, 2013–2014) with a large number of consolidation and upgrade activities. Run 2 started in 2015 and is planned to continue until the end of 2018. The main accelerator goals of Run 2 are to produce more than 100 fb^{-1} of data. The parameter archived (by June 2016) are shown in Table 3 [51]. Figure 5 shows the integrated delivered luminosity per year in the LHC.

3.2 The ATLAS detector

The ATLAS (A Toroidal LHC ApparatuS) detector, which gives the name to the experiment and collaboration, is the largest volume detector ever constructed for a particle

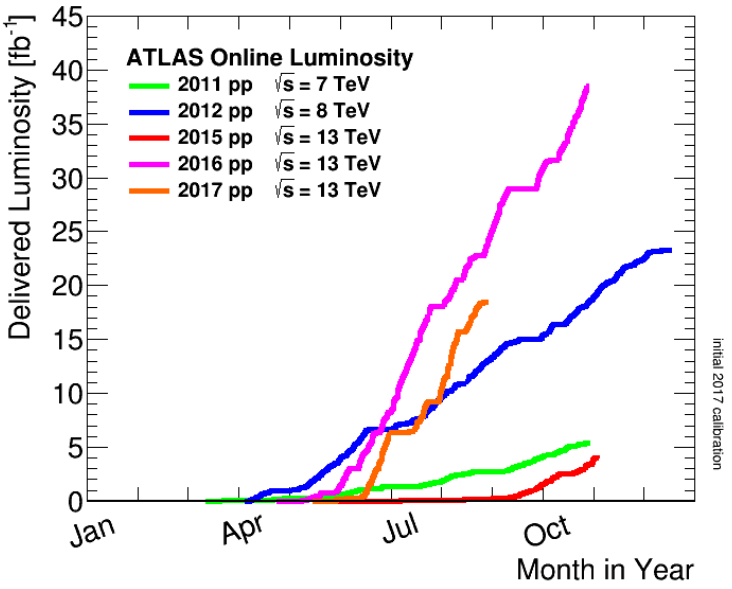

Figure 5: Cumulative luminosity versus day delivered to ATLAS during stable beams and for high energy p-p collisions [52].

collider. It investigates a wide range of physics, from the search of extra dimensions to dark matter. Sat in a cavern 100 m below ground, it has the dimensions of a cylinder, 46 m long, 25 m in diameter. The ATLAS detector weighs 7.000 tonnes[5].

As can be seen in Figure 6, ATLAS detector is composed by six different subsystems: The Inner Detector sorrounded by the Solenoidal Magnet, the Electromagnetic and Hadronic calorimeters, the Toroid Magnets and the Muon Spectrometer [53].

The coordinate system of ATLAS has its origin at the collision point, at the center of the detector. The beam axis defines the Z-axis, the direction from the origin to the center of the ring gives the X-axis and the orthogonal to the others axis is the Y-axis, which points upwards. The azimuthal angle, ϕ, is measured around the X-axis and the polar angle, θ, respect to the beam axis. The latter is used to define the pseudorapidity (Figure 7), which is a purely geometrical quantity that depends on the polar angle θ, but not on the particle's mass:

$$\eta = -ln \tan\left(\frac{\theta}{2}\right) \tag{12}$$

The forward part of the detector is the one with large values of $|\eta|$. The part of the detector with $Z > 0$ is called *Side A*, while $Z < 0$ is named *Side C*. The subsystems parallel to the Z-axis form what is called the barrel of the detector. On the two sides of the barrel there are the end-caps, these are the detecting elements which are arranged in transversal planes to the beam axis.

[5]This is similar to the weight of the Eiffel Tower.

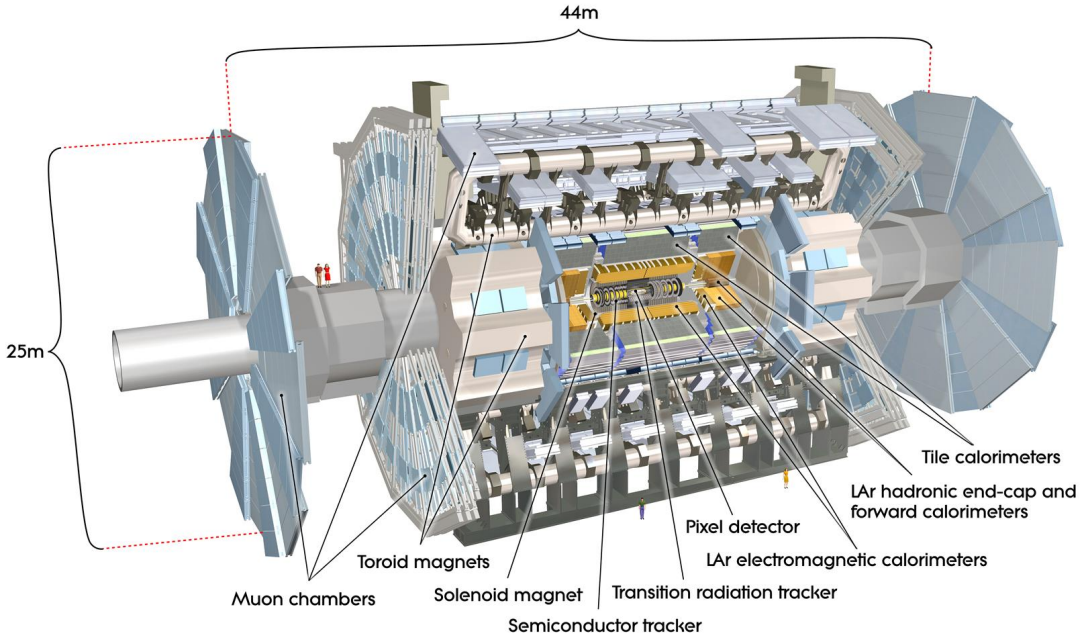

Figure 6: The ATLAS detector layout with all its subdetectors.

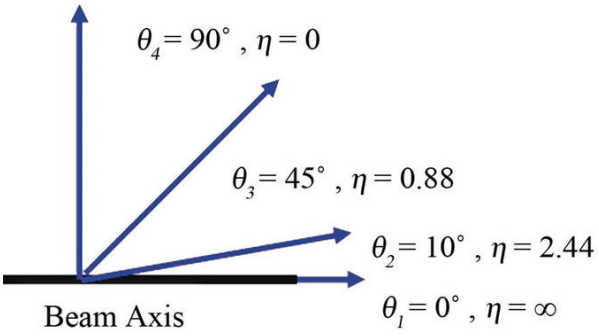

Figure 7: Pseudorapidity (η) values on a polar plot. A $\theta = 0$ corresponds to the beam axis.

Inner detector

The inner detector (ID) is the innermost part of the detector. Beginning only a few centimetres from the proton beam axis, consists in a cylinder with a radius of 1.05 m and a length of 7 m. It is intended mainly to detect charged particles inside the range $|\eta| < 2.5$, revealing its position and momentum, i.e. to reconstructs its traces. It is also used to identify the type of particle, reconstruct the primary vertices and particles such as electrons or jets from b-quark hadronization. It is composed of three different and independent subdetectors: the Pixel detector and the semiconductor tracker (SCT), which are precision tracking detectors, and the straw tubes of the transition radiation tracker (TRT). The general function of each system is to record a "hit" when a particle passes through a certain point across it. The momentum resolution of the ID is $\frac{\sigma_{pT}}{p_T} = 0.05\% \oplus 1\%$ for $p_T < 1$ TeV.

- Pixel detector: It is innermost part of ID. Having a high granularity, it provides

a very high precision set of measurements close to the interaction point. Contains four layers in the barrel and three disks on each end-cap; in total there are 1744 modules with size of 2 cm by 6 cm. The material for the detection is semiconductor silicon.

- SCT: The next part is conceptually similar but with long and narrow strips of 80 μm by 12.6 cm instead of pixels, which translates into a larger coverage area. Since it measures particles over a much larger volume than the previous layer, it is the most important part of the detector when it comes to track the particles in the plane perpendicular to the beam.

- TRT: The last part of the ID is formed by layers of gaseous straw tube elements and transition radiation material. The TRT provides electron identification capability through the detection of transition radiation X-ray photons.

Calorimeter

The energy of the particles is measured by the calorimeters. Situated outside the solenoidal magnet that surrounds the ID, the calorimeter covers all the azimuthal angle and a range of $|\eta| < 4.9$. Its basic function is to absorb the energy of both charged and neutral particles in order to measure it. This part of ATLAS is divided in two subdetectors: an inner electromagnetic calorimeter (ECal) and the hadronic one (HCal).

The calorimeters use alternating layers of absorber and active material. The incident particle produces a shower of secondary particles when it interacts with the material. The energy of the showers is detected when it is deposited in the active material. Liquid Argon (LAr) was chosen as the main active material for the calorimeter due to its intrinsic linear behaviour and radiation hardness, other parts use plastic scintillators. The only particles that scape from calorimeters are the muons and the neutrinos; the former ones are detected in the muon system and the latter leaves the detector without interacting.

ECal : It is the inner of the two calorimeters. Its barrel region provides high granularity for precision measurements of electrons, positrons and photons. Mostly made by LAr, the ECal absorbs energy from particles that interact electromagnetically (photons and electrically charged). The showers in the LAr liberate electrons that are collected and recorded later. The barrel part covers $|\eta| < 1.475$ and the two endcap components cover a range of $1.375 < |\eta| < 3.2$. It has great precision in the location of the energy deposition and its amount. The expected energy resolution of the ECal is $\frac{\sigma_E}{E} = \frac{10\%}{\sqrt{E}} \oplus 0.7\%$ in the energy range $10 < E < 245$ GeV.

HCal : Surrounding the ECal there is the HCal, which provides information about the particles that pass through the latter and are strongly interacting (the hadrons). This calorimeter is less precise in magnitude and location than the ECal. It is composed by three subdetectors: a Tile calorimeter (TileCal), a LAr hadronic endcap (HEC) and LAr forward calorimeter (FCal).

TileCal : Placed directly outside the ECal, it covers $|\eta| < 1.7$. Its active material is scintillating plastic tiles and its absorber is steel. The tiles are illuminated by the hadronic showers and the light is recorded. The expected energy resolution for the barrel and endcap calorimeters is $\frac{\sigma_E}{E} = \frac{50\%}{\sqrt{E}} \oplus 3\%$ for single pions of energy $10 < E < 300$ GeV.

HEC : It consists of four wheels, two in each endcap, built from parallel copper plates with 8.5 mm LAr gaps. It overlaps with the forward calorimeter in the range of $3.1 < |\eta| < 3.2$ and with the TileCal in $1.5 < |\eta| < 1.7$.

FCal : Situated near the pipe ($3.1 < |\eta| < 4.9$), consists of three modules in each endcap: A copper one for electromagnetic measurements and two of tungsten for hadronic energy interactions measurements. Its expected energy resolution is $\frac{\sigma_E}{E} = \frac{100\%}{\sqrt{E}} \oplus 10\%$ for single pions in $10 < E < 300$ GeV energy range.

Muon system

The Muon Spectrometer (MS) is the outermost part of the ATLAS detector and its aim is to detect charged particles escaping from the barrel and endcaps calorimeters. The MS measures the momentum of these particles in the $|\eta| < 2.7$ range. Muons are the only particles that can reach the MS and be detected. The MS measures the trajectories of the muons to determine its momentum and charge sign with precision. This measurement takes place inside a magnetic field produced by superconducting toroid magnets. The muon chambers are made of thousands of metal tubes equipped with a central wire and filled with gas. When a muon passes through the these tubes, it leaves a trail of electrically charged ions and electrons which drift to the sides and center of the tube. The position of the muon is, therefore, determined from the time that it takes to these charges to drift. The MS is equipped with four different kind of chambers: Monitored Drift Tube chambers, Cathode Strip Chambers, Resistive Plate Chambers and Thin Gap Chambers. The first two are used for precision measurements of mass and the other for the trigger and data acquisition. It is designed to achieve a resolution below 4% for muons with transverse momentum $p_T < 2$ GeV, if $p_T = 1$ TeV the resolution increases to 10%.

Trigger and data acquisition system

The proton bunches travel almost at the speed of light and they collide at the center of the detector 40 million times per second, i.e. 40 MHz or every 25 ns. Since reading out and storing all the information ($\sim$ 100 TB/s) is not feasible, ATLAS uses a complex and highly distributed Trigger and Data Acquisition (TDAQ) system, in charge of selecting only interesting data and transporting those to permanent mass storage ($\sim$ 1 GB/s) for later analysis. This reduction is carried out in two stages: The electronic performs a initial selection and then a large computer farm analyses the data that pass the initial filter.

ATLAS subdetectors make several filterings. The Level 1 (L1) Trigger performs a first rejection based on simple calorimetry and muon tracking information by reducing the data by a factor of 100. It is a hardware trigger that decreases the amount of

information accepted rate to 75 kHz. After the L1 the data is stored in large memory buffers ($\sim 17 \times 10^3$ cores) in the Read-Out system (ROS) for further real time analysis in the High Level Trigger (HLT) farm. The HLT is consists in two steps. The first step is the L2, that uses the regions of interest defined by L1 to further reduce the event rate to 1 kHz. The second step is the event filter, which has access to full detector granularity and reduces the output to approximately 400 Hz. The surviving data is stored for later physics analyses [54].

4 Analysis tools

4.1 Simulated event samples

To perform a precise measurement of the angular distributions and asymmetries described in Section 2 with the purpose of explore the possible presence of anomalous couplings in the Wtb vertex, accurate MC models predicting the characteristics of the expected data are needed for both the signal and SM background precesses. All simulation samples are passed through the MC simulation of ATLAS detector [55] based on GEANT4 [56]. Since the final observable is an angular distribution, which is highly sensitive to kinematic mismodelling, special care must be taken in this analysis [57].

The single-top-quark production in the t-channel sample is produced combining the NLO MC generator POWHEG [58] and the general purpose MC generator PYTHIA8 [59] for the parton shower, fragmentation and the underlying event. The simulation includes both the $q + b \to q' + t$ and $q + g \to q' + t + \bar{b}$ diagrams (Figure 1-b).

The background processes are those which mimic the experimental signature of t-channel single-top-quark events. These can be classified in four main groups:

- Top quark pair ($t\bar{t}$), s-channel and Wt-channel: production of top quarks via strong interactions and other channels of electroweak production.
- W+jets: production of a real W boson in association with heavy- or light-flavour jets.
- Z+jets: electroweak production of single Z boson and diboson.
- Multijet: events from QCD multijet production where one jet is identified as a lepton and a mismeasurement creates large E_T^{miss}.

The W and Z bosons are simulated with SHERPA2.1.1 generator [60], in which matrix elements up to two partons are calculated at NLO while LO calculations are used for 3 and 4 partons. The CT10 parton distribution function (PDF) set is used. The W+jets and Z+jets processes are normalised to their NNLO prediction. The backgrounds $t\bar{t}$, single-top s-channel and Wt processes, are simulated using POWHEG generator with PYTHIA8 for the parton shower, fragmentation and the underlying event as it has been done for the signal t-channel events. Diboson production, including WW , WZ and ZZ

is simulated with Sherpa2.1.1 with the CT10 PDF set. In Table 4 is shown how these processes are generated.

Process	Generator	PDFs
Single top		
t-channel	POWHEG+PYTHIA	CT10
s-channel	POWHEG+PYTHIA	CT10
Wt	POWHEG+PYTHIA	CT10
$t\bar{t}$	POWHEG+PYTHIA	CT10
$W \to l\nu + jets$	POWHEG+PYTHIA	CT10
$Z \to \nu\nu, ll + jets$	POWHEG+PYTHIA	CT10
Diboson		
WW	SHERPA	CT10
WZ	SHERPA	CT10
ZZ	SHERPA	CT10

Table 4: List of MC generators and PDFs used for the different signal and background processes that have been simulated.

The multijet background is the only process that is not determined though a MC simulation, for this events the data-driven matrix method has been used [15]. This method [61] allows to estimate the number of multijet background events in the signal region by deriving the true composition of the data sample in terms of prompt (real) and fake leptons from its observed composition in terms of tight (signal selection) and loose leptons. The loose lepton selection consist of identical requirements as for those applied to the tight signal sample but relaxing the identification criteria on the leptons, electrons or muons, mainly relaxing the lepton isolation requirements. The stringent tight selection is a subset of the lax loose selection. The number of multijet events N_{fake}^{tight} passing the signal requirements can be expressed as:

$$N_{fake}^{tight} = \frac{\epsilon_{fake}}{\epsilon_{real}}(N_{data}^{loose} \cdot \epsilon_{real} - N_{data}^{tight})$$

where ϵ_{real} real and ϵ_{fake} are the efficiencies for real and fake loose leptons being selected as tight leptons, $N_{data}^{loose} = N_{real}^{loose} + N_{fake}^{loose}$ is the number of selected events in the loose sample, and $N_{data}^{tight} = N_{real}^{tight} + N_{fake}^{tight}$ is the number of selected events in the signal sample. The fake-lepton efficiencies are determined from a data sample dominated by non-prompt and fake-lepton background events. The real-lepton efficiencies are also estimated from collision data using a "tag-and-probe" method in $Z \to ee$ events.

4.2 Object reconstruction

The objects to be reconstructed in this analysis are the electrons, jets and E_T^{miss}. The electron and the neutrino (E_T^{miss}) come from the decay of the W boson and the jets

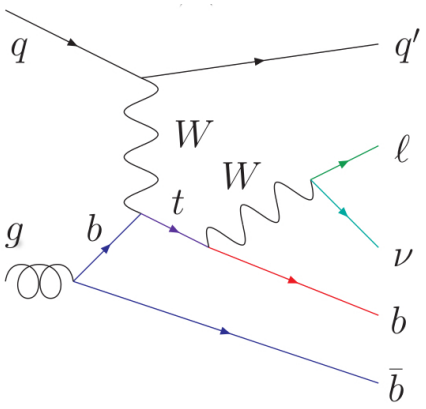

Figure 8: Representative Feynman diagram for t-channel single-top-quark production and decay.

arise from the quarks, these are the elements present at the final state in the top quark production and decay in the t-channel, as can be seen in Figure 8.

Electron candidates are identified as clusters of energy deposited in the electromagnetic calorimeter with a well measured track [62] [63]. They are required to have a $p_T > 30$ GeV and the cluster must yield in the region defined by the pseudorapidity range of $|\eta_{clus}| < 2.47$, excluding the region $1.37 < |\eta_{clus}| < 1.52$. In order to reduce background events in which a hadronic jet is misidentified as a prompt electron or electrons from the decay of heavy quarks, isolation criteria are applied. These criteria are optimised such that, by adjusting the isolation threshold, the selection efficiency of the isolation criteria is uniform across the η of the electron. This efficency increases from 90% for $p_T = 25$ GeV to 99% for $p_T = 60$ GeV [15]. In addition, all tracks (excluding the track belonging to the electron) in a cone of size $\Delta R = \sqrt{(\Delta\eta)^2 + (\Delta\phi)^2} = 0.3$ around the electron direction have a restriction of p_T below a threshold dependig on the electron tranverse momentum. Finally, a calorimeter isolation in a cone of size 0.2 around the electron is required [64].

Jets are reconstructed with the so called anti-k_t algorithm [65] with a radius parameter[6] of 0.4. This method is a successive recombination algorithm that inverts the parton shower be combining the constituents of the jet according to distance criteria weighted by relative transverse momentum. The calibration is done using a combination of data and a simulation depending in the energy and the $|\eta|$ [66]. Only jets with $p_T > 30$ GeV and $|\eta| < 3.5$ are accepted. The rapidity range is determined using a region dominated by W+jets and by requiring a good agreement between simulated a measured data.

When there are jets close to an electron in the $\Delta R < 0.2$ range, the closest jet is removed because both, the electron and jet, are likely to correspond to the same physical object. The remaining electron candidates overlapping with jets within $\Delta R < 0.4$ are subsequently rejected.

To discriminate between jets from hard-scatter processes and those from pile-up, the jet vertex tagger (JVT) is used as a discriminant [67]. It is constructed from tracking and vertex information using a two-dimensional likelihood method. The JVT variable is

[6]The R in distance parameter $d_{ij} = min(k_{T,i}^{2P}, k_{T,j}^{2P})\frac{R_{ij}^2}{R^2}$, being R_{ij} the distance between to objects in the $\eta - \phi$.

required to be more than 0.64 for jets with $p_T > 50$ GeV and $|\eta| < 2.4$, corresponding to an efficiency of 92% and a misidentification rate of 2%.

In this analysis it is important to identify the b-jets[7]. With that purpose we use a b-tagging algorithm, based on boosted decisions trees which is optimised to reject c-jets as well as light quark jets. This algorithm can only be applied to jets with the coverage of the ID. The b-tagging efficiency is extracted from $t\bar{t}$ simulated events and it is 60%. 0.06 % of light-quark jets and 4.7 % of c-quark jets are mistagged as b-quark jets [15].

The magnitude of the missing transverse momentum is a measure of the momentum imbalance in the plane transverse to the beam axis due to the escaping neutrinos. It is defined as $E_T^{miss} = |\overrightarrow{E_T}^{miss}|$, where the vector $\overrightarrow{E_T}^{miss}$ is obtained using the reconstructed three-dimensional calorimeter energy clusters associated with the selected jets together with either the calibrated calorimeter energy cluster associated with an electron or the p_T of a muon track. Contributions from soft particles not associated with the identified ones, are accounted for using tracks associated to vertex but not associated with a jet or electron [15].

4.3 Trigger requirements and event preselection

The experimental signature of t-channel single top-quark events in the single lepton channel consists of one isolated charged lepton from the W-boson decay, large E_T^{miss} due to the neutrino coming from the leptonically decaying W boson, exactly two jets and one of them identified as likely to be originated from the fragmentation of the b-quark coming from the top-quark decay. Then, the remaining jet would be the forward jet originated by the fragmentation of the spectator quark.

In this master thesis we have analysed only the electron channel due to technical reasons of availability of the analysis samples at the time of the research work was developed. Along with the trigger requirements, the preselection requirements summarised in Table 5 are applied. This set of cuts is implicitly applied in all the further set of cuts used in this work.

Only events passing the single-electron trigger are considered [68] [15]. The L1 (subsection 3.2) requirement demands a E_T deposit above 20 GeV with a reduced calorimetric granularity being considered at this stage. Events in the electron channel are triggered by a calorimeter cluster matched to a track, and the trigger electron object is required to have either $E_T > 60$ GeV or $E_T > 24$ GeV and satisfy some isolation criteria. Only events containing exactly one isolated charged lepton with $p_T > 30$ GeV and $|\eta| < 2.5$ are accepted. Candidate events must have exactly two jets satisfying the criteria described in Section 4.2. Jets reconstructed in the range $2.75 < |\eta| < 3.5$, covering the endcap-forward calorimeter transition region, must have $p_T > 35$ GeV. One of the selected jets is required to be identified (b-tagged) as a b-jet.

In order to reject a part of the multijet background events, which are charac-

[7] Jets corresponding to the hadronization of a b-quark.

terised by low E_T^{miss} and the transverse mass of the W-boson $m_T(W)$[8], the event selection requires $E_T^{miss} < 30$ GeV and $m_T(W) > 50$ GeV. To further suppress the multijet background a requirement on the p_T of the charged lepton and the azimuthal angle between the charged lepton and jet is applied [15] [69]:

$$p_T(l) > 40 \left(\frac{|\Delta\phi(j_1, l)| - 1}{\pi - 1} \right) \text{GeV},$$

where l denotes the charged lepton and j_1 the reconstructed jet with the highest p_T.

A dilepton veto is applied to reject dileptonic sources of background, mainly $t\bar{t}$ dileptonic events. Therefore, contributions from processes with two isolated leptons in the final state are suppressed by rejecting any event with an additional electron or muon as defined above satisfying $p_T > 10$ GeV. This cuts are summarised in Table 5.

Preselection cuts
Single lepton trigger
Primary vertex ≥ 5 tracks
Exactly 1 lepton with $\|\eta\| < 2.47$ and $p_T > 30$ GeV
2 jets with $p_T > 30$ GeV and $\|\eta\| < 3.5$
1 b-jet
$E_T^{miss} > 30$ GeV
$m_T(W) > 50$ GeV

Table 5: Preselection requirements. These cuts are implicitly applied in all further selections.

After imposing the preselection cuts of Table 5 over the 13 TeV simulated samples for t-channel single-top-quark production with the leptonic decay of the top quark to an electron, we get the event yields presented at Table 6. Given the small fraction of signal events in the dataset at preselection level, further requirements are applied to separate the signal from the background. From now on, the errors on the event yields presented at Tables 6, 7, 8, 9, 10, 11 and 12 account only for the statistical precision of the MC.

5 Optimisation of the selection criteria of t-channel single-top-quark events at $\sqrt{s} = 13$ TeV

In this section we are going to design a set of selection cuts to be required on top of the pre-selection criteria described in the previous Section 4 in order to enhance the single-top-quark t-channel signal content and the rejection of SM background processes and ultimately to obtain a data sample suitable to explore the Wtb vertex through the measurement of top-quark and W-boson polarisation observables.

[8]Defined as $m_T(W) = \sqrt{2p_T^l E_T^{miss}[1 - \cos(\phi^l - \phi^{E_T^{miss}})]}$, being p_T^l the transverse momentum of the lepton, ϕ^l its azimuthal angle and $\phi^{E_T^{miss}}$ the azimuthal angle of the E_T^{miss}.

Process	Event yield	Bkg fraction
t-channel	41154 ± 127	-
Z-jet, diboson	10217 ± 239	3.0%
W+jets	151047 ± 1748	44.5%
$t\bar{t}$	119770 ± 230	35.2%
Wt s-channel	27580 ± 123	8.1%
Multijet	31171 ± 175	9.2%
Total	380940 ± 1796	-
S/B	0.121	
Significance	67	

Table 6: Event yields obtained when applying the preselection requirements over the 13 TeV MC samples. Electron channel only.

The strategy follow in the choice of these requirements comprise three arguments:

First, to exploit the topology of single-top-quark t-channel events in order to increase the signal content and reject background events from SM processes. Second, these requirements should be placed on event variables that do not depend on individual kinematic properties of the reconstructed decay products of the top quark since these last ones are involved in the measurement of the angular observables to be used in the exploration of the Wtb vertex. This second argument is based on the experience gained from the Run I analyses [13] and [24] and it is aiming to avoid potential biases that the selection could introduced in the efficiency measured with signal MC samples with non-zero values of the anomalous couplings in the Wtb vertex. These samples have been employed in the past to test the linearity of the response of the whole analysis chain to the presence of signal events with anomalous couplings. A recent measurement of the inclusive cross-section of single top-quark t-channel production at 13 TeV by ATLAS [15] has used a neural network to discriminate signal events over background events. However, some of the variables considered in this neural network have been build using kinematic properties of one or two of the decay products of the top quark and, therefore, could again bias the measurements of the angular distributions of the top decay products.

Lastly, after having chosen the selecting variables, the actual numerical values of the cuts need to be optimised in terms of the significance.

Significance

The parameter that we try to maximise is the significance, which is suggested in [70] for optimisation purposes when knowing explicitly the cross section of the searched signal, as it is the case of the single top t-channel signal:

$$Significance(S, B) = \frac{S}{\sqrt{S+B}}$$

where S is the number of events of the signal (t-channel) and B is the number of background events. The significance as a quantity to maximise, is a frequently used parameter in particle physics. It is not maximised with the actual data, but with simulated data, or MC for short, and/or orthogonal datasets.

Most measurements in particle physics are basically a counting exercise, so the are subject to Poisson statistics. In a Poisson distribution, variance is equal to the number counted ($N = S + B$), therefore standard deviation is $\sqrt{N}$. The significance may be understood as the size of the signal relative to one standard deviation ($S/\sqrt{N}$). Which means that one will get a better result as the statistics increase. This is useful for an analysis, because when a set of cuts is chosen it is necessary a way to account for how much statistics have been left with after the cuts. Optimising using $S/\sqrt{S+B}$ accounts for this: if the cuts are too tight in trying to optimise S/B, one might not have enough statistical significance. This reasoning fails when N is small, because the approximation implicit in using the standard deviation of the Poisson distribution rapidly becomes invalid. Fortunately this is not a problem in accelerator physics experiments, where the number of events is large.

5.1 Baseline selection from $\sqrt{s} = 8$ TeV analyses

The starting point of our studies would be the selection carried out in the most recent ATLAS analyses of the Wtb vertex using t-channel single-top-quark events: [13] and [24] produced in pp collisions at $\sqrt{s} = 8$ TeV. In these analyses, four variables were used with the next choice of cuts that were optimised using signal and MC samples produced at $\sqrt{s} = 8$ TeV:

- m_{top}: The reconstructed top mass is built from the invariant mass of the lepton (electron), the b-jet and the neutrino. The transverse coordinates of the neutrino momentum p_x^ν and p_y^ν are assumed to be measured from the x and y component of the E_T^{miss}. The longitudinal momentum of the neutrino p_z^ν is obtained from the method described in Appendix A of [71].
- H_T: The scalar sum of all the transverse energy of all final objects involved. This quantity is defined as[9] $H_T = p_T^l + p_T^j + p_T^b + E_T^{miss}$.
- $|\eta_j|$: Absolute value of the pseudorapidity of the light jet, η_j.
- $\Delta\eta_{j,b}$: The distance in η between the light jet, i.e. spectator quark, and the b-jet. This distance must be large.

The $\sqrt{s} = 8$ TeV selection, i.e. set of cuts, demands that the reconstructed mass of the top quark yields in $m_{top} \in [130, 200]$ GeV to reject background events from processes not involving the top quarks. The transverse energy of the final objects has an upper cut of $H_T > 195$ GeV in order to reduce the W+jets background contribution. The pseudorapidity of the light jet must satisfy $|\eta_j| > 2.0$, since the spectator quark tends to

[9] The upper index j stands for the light jet and the b for the b-jet.

be produced in the forward direction in the t-channel process. Finally, in order to reduce the contribution from top-quark pair production background events, a pseudorapidity separation between the b-jet and the light jet must be $\Delta\eta_{j,b} > 1.5$.

In Table 7 we compare the signal and background event yields that we have obtained by applying the selection used in the 8 TeV analyses to the MC samples at 13 TeV enumerated at Table 4. Due to the combined effect of two facts: the increased integrated luminosity properly considered in the normalization of the event yields together with the increased cross sections of the signal and background processes considered in their generation, the S/B ratio decreases from 1.32 down to 0.65 and the significance increases from 39 up to 71. This is not surprising since the 8 TeV selection is not optimised for the 13 TeV samples.

Process	Event yield (13 TeV)	Bkg fraction (13 TeV)	Event yield (8 TeV)	Bkg fraction (8 TeV)
t-channel	14181 ± 75	-	2663 ± 14	-
Z-jet, diboson	823 ± 73	3.9%	80 ± 5	4.0%
W+jets	8831 ± 644	41.6%	783 ± 30	38.9%
$t\bar{t}$	8237 ± 61	38.8%	849 ± 7	42.2%
Wt s-channel	1366 ± 26	6.4%	100 ± 8	5.0%
Multijet	1986 ± 50	9.3%	176 ± 123	8.7%
Total	35424 ± 658	-	4676 ± 128	-
S/B	0.650		1.32	
Significance	71		39	

Table 7: Comparison of the event yields obtained when applying the 8 TeV selection over the 13 TeV MC samples against the ones from the analysis [13], i.e. the 8 TeV samples. Only the electron channel is considered.

One could work from this selection to tune the values of the cuts and hence enhance the significance and the S/B ratio but there is a major problem with this choice of variables. The hurdle is that the $\Delta\eta_{j,b}$ is related to the kinematics of the decay products of the top quark and, as explained before, this could bias the measurements.

5.2 Cut in $m_{l,b}$

An upper cut in the variable $m_{l,b}$, i.e, the invariant mass of the lepton and the b-jet, is motivated for two reasons. The first one is the background rejection, as it can be seen it Figure 9.

The second one is to exclude the off-shell region of the top-quark decay beyond the kinematic limit of $m^2_{l,b} = m^2_{top} - m^2_W$, being m_W the mass of the W-boson. The reason behind was that the off-shell region was not well modelled by the MC generators since off-shell effects are not included in the underlying matrix-element calculation [72].

The upper cut in $m_{l,b}$ has been chosen to account for the considerations described in previous paragraphs and at the same time to avoid introducing potential biases when measuring the angular distributions, specially $\cos(\theta^*_l)$ related the helicity fractions of the

W boson (Section 2.2) that has a clear dependence on $m_{l,b}$:

$$m_{l,b}^2 = \frac{m_{top}^2 - m_W^2}{2}[1 - \cos(\theta_l^*)]$$

In Figure 10 it can be seen that a cut down to $m_{l,b} < 140$ GeV is safe and does not affect the parabolic dependence of $\cos(\theta_l^*)$ in $m_{l,b}$.

In Figures 22, 28 and 34 in Apendix A it can be seen that also the other angular distributions, $\cos(\theta_l)$, $\cos(\theta_{LX})$ and $\cos(\theta_{LY})$ are not correlated with $m_{l,b}$ and thus not affected by this cut.

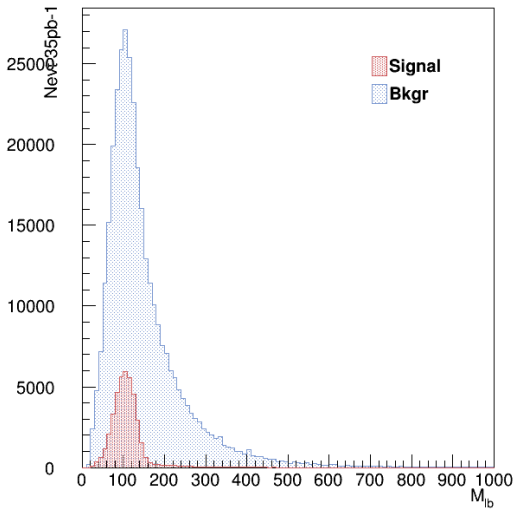

Figure 9: $m_{l,b}$ distribution at preselection level for the electron channel.

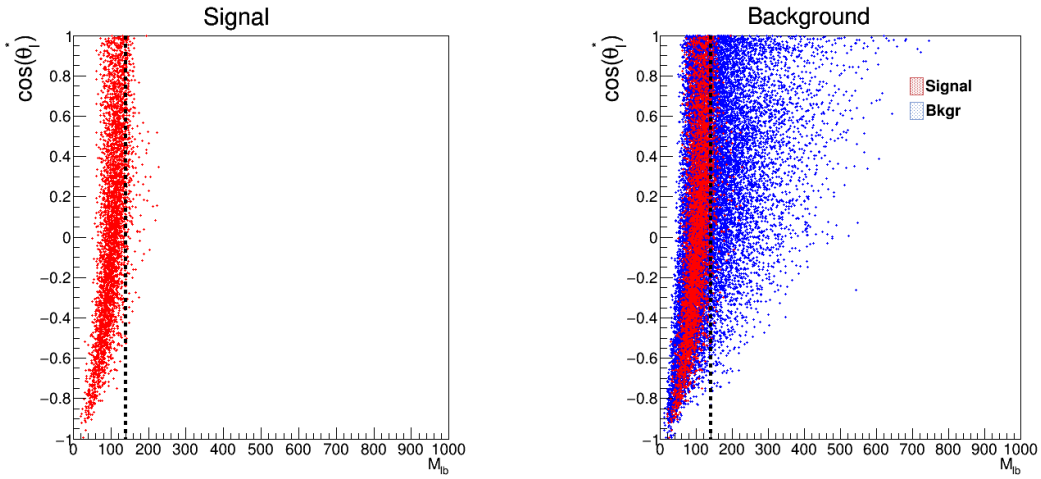

Figure 10: Scatter two-dimensional plot were the signal (background) has been scaled by a factor 0.1 (0.05) for aesthetic purposes of $\cos(\theta^*)$ versus $m_{l,b}$ at preselection level for the electron channel. The doted line denotes the upper cut.

The event yields after applying the cut on $m_{l,b}$ are in Table 8, there can be seen that the significance and the S/B have grown with respect to the preselection level. The significance has grown from 67 up to 75 and the S/B from 0.121 to 0.181.

Process	Event yield	Bkg fraction
t-channel	36988 ± 120	-
Z-jet, diboson	5500 ± 210	2.7%
W+jets	87948 ± 1451	43.1%
$t\bar{t}$	80409 ± 188	39.4%
Wt s-channel	18061 ± 98	8.9%
Multijet	12124 ± 107	5.9%
Total	241030 ± 1490	-
S/B	0.181	
Significance	75	

Table 8: Event yields and background fractions after preselection and requiring $m_{l,b} < 140$ GeV for MC 13 TeV samples. Electron channel.

5.3 Optimisation of the m_{top} window

The second condition to be applied is over the mass of the top quark, its distribution is shown in Figure 11. Cutting on m_{top} is used to remove from the data events which do not have a real top: Z-jet, diboson, W+jets and multijet. But this is not helpful to clean the background of events such as $t\bar{t}$ or Wt vertex in s-channel.

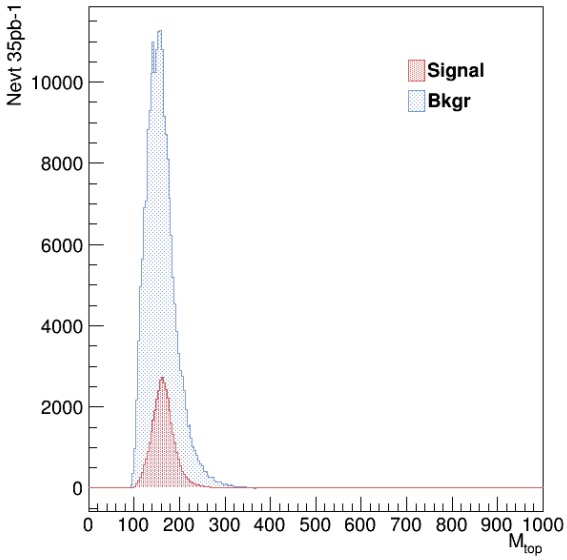

Figure 11: m_{top} distribution after preselection and $m_{l,b}$ cuts.

Starting from the one dimensional distribution of m_{top} we have built two dimensional maps of significance and S/B by sweeping simultaneously the lower and the

upper requirement on m_{top} in the ranges shown in the X and Y axes of Figure 12. At a given point ($m_{top}(lower)$, $m_{top}(upper)$) of these two dimensional maps, significance and S/B have been obtained from the integral of the one dimensional distributions signal and background distributions in the range: $m_{top}(lower) < m_{top} < m_{top}(upper)$.

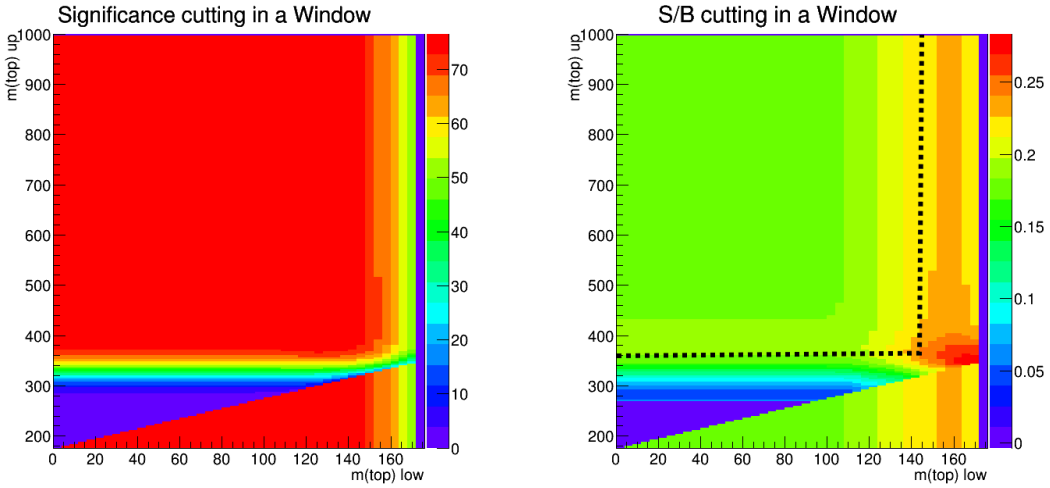

(a) Significance (b) S/B ratio

Figure 12: Two dimensional histograms showing significance and S/N ratio for m_{top} with lower and upper cuts. The doted line in (b) delimit the area in which the significance is maximum.

In Figure 12-(a), can be seen that the maximal significance criteria is satisfied with any upper cut above 360 GeV and lower below 147 GeV. Then we pay attention at Figure 12-(b) to look for the point that, satisfying the previous condition, maximises the S/B ratio. Scanning the values of significance and S/B for all bins between 140 GeV and 160 GeV for the lower cut and 350 GeV to 450 GeV for the upper, we find that the optimum limits for the m_{top} are:

$$m_{top}(lower) = 142 \text{ GeV}$$
$$m_{top}(upper) = 418 \text{ GeV}$$

The peak of the top mass is on its theoretical value, 175 GeV, which lays inside the window defined by the cuts. Table 9 shows the event yields after demanding that the conditions $m_{l,b} < 140$ GeV and $m_{top} \in [142, 148]$ are satisfied. As expected, all backgrounds that do not contain a real top have lost relevance regarding the background fraction: the Z-jet and diboson from 2.7% to 2.2%, the W+jets from 43.1% to 38.1% and the multijet from 5.9% to 4.1%.

5.4 $\Delta\eta_{j,top}$ and $|\eta_j|$ triangular cut

In the case of the variables $\Delta\eta_{j,top}$ and $|\eta_j|$ (Figure 13), the two-dimensional correlation shown in Figure 14 suggested a triangular cut of the form: $|\eta_j| > \eta_{j0} - \Delta\eta_{j,top}$, with η_{j0} to be optimised. The event yields, background fractions, significances and S/B ratios, obtained after applying the preselection, $m_{l,b}$, m_{top} and triangular cut are shown in Table 10 for different values of η_{j0}. For maximasing the significance, $\eta_{j0} = 3.0$ is the best

Process	Event yield	Bkg fraction
t-channel	30477 ± 109	-
Z-jet, diboson	3094 ± 134	2.2%
W+jets	53180 ± 1085	38.4%
$t\bar{t}$	62880 ± 166	45.4%
Wt s-channel	13780 ± 86	9.9%
Multijet	5675 ± 79	4.1%
Total	169086 ± 1117	-
S/B	0.220	
Significance	74	

Table 9: Event yields after preselection, $m_{l,b} < 140$ GeV and $142 < m_{top} < 418$ GeV requirements for 13 TeV MC samples. Only the electron channel is considered.

choice but, nevertheless, we are using we take $\eta_{j0} = 3.5$ because we have a gain in S/B of 19% compared to the $\eta_{j0} = 3.0$ case by only loosing a 1.3% of significance. The S/B ratio has been doubled with this new cut.

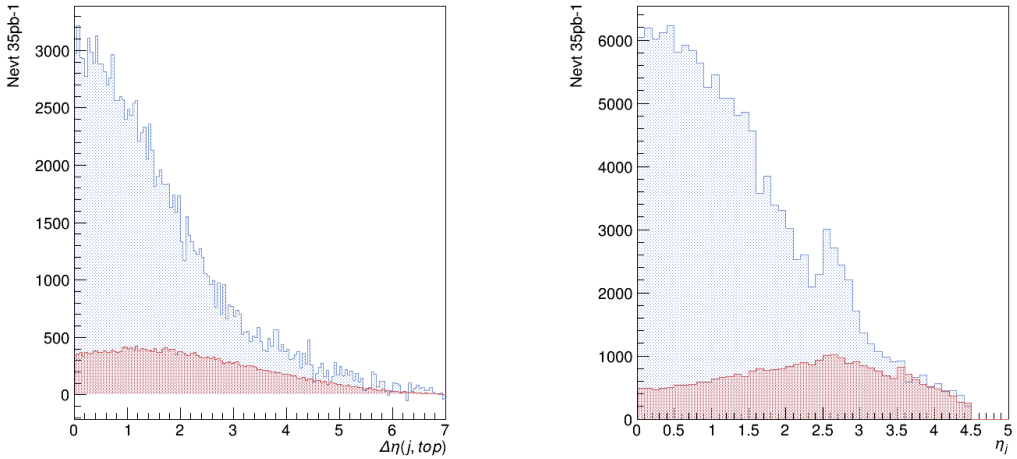

(a) $\Delta\eta_{j,top}$ (b) $|\eta_j|$

Figure 13: Distribution of (a) $\Delta\eta_{j,top}$ and (b) $|\eta_j|$ after applying the cuts in $m_{l,b}$ and m_{top}. Electron channel. The red area is the signal wihile the blue is the background.

5.5 Two dimensional optimisation of H_T and $m_{j,top}$, requirements

The S/B and significance obtained after preselection, $m_{l,b} < 140$ GeV, 142 GeV $< m_{top} <$ 418 GeV and $|\eta_j| > 3.5 - \Delta\eta_{j,top}$ could be improved further improved with further requirements. At this stage, we consider a two dimensional optimisation of two variables that do not depend on kinematic properties of individual top quark decay products: H_T and $m_{j,top}$.

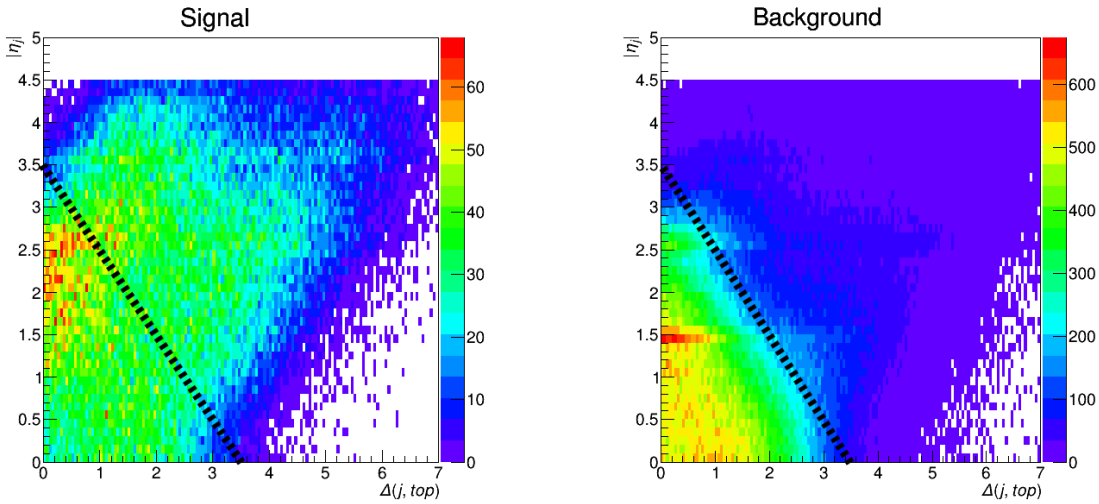

Figure 14: Two-dimensional correlation between $|\eta_j|$ and $\Delta\eta_{j,top}$ after the cuts in m_{top} and $m_{l,b}$ have been applied. The area below the doted line is removed from the selection.

Process	Event yields		
	$\eta_{j0} = 2.8$	$\eta_{j0} = 3.0$	$\eta_{j0} = 3.5$
t-channel	23008 ± 94	21942 ± 92	19259 ± 86
Z-jet, diboson	1722 ± 110	1547 ± 106	1126 ± 93
W+jets	26521 ± 924	23692 ± 901	18422 ± 809
$t\bar{t}$	23914 ± 103	20706 ± 96	14498 ± 80
Wt s-channel	4677 ± 51	3944 ± 46	2687 ± 38
Multijet	4292 ± 72	3957 ± 69	2961 ± 58
Total	84134 ± 946	75788 ± 921	58954 ± 825
S/B	0.376	0.408	0.485
Significance	79	80	79

Table 10: Keeping events with $m_{l,b} < 140$ GeV and $142 < m_{top} < 418$ GeV and a cut of the form $|\eta_j| > \eta_{j0} - \Delta\eta_{j,top}$ for 13 TeV samples.

Starting from the two dimensional distribution of $m_{j,top}$ versus H_T we have built two dimensional maps of significance and S/B using a two dimensional integration by sweeping simultaneously: $H_T > H_T(min)$ and $m_{j,top} > m_{j,top}(min)$.

Later, we maximise the significance by iterating over the bins of the previous significance map in Figure 16 searching for the maximum value of significance and keeping a fixed working point of minimum S/B required.

Afterwards, we keep various fixed working points of minimum S/B and maximise the significance. From the map of significances, these points are identified for five boundary cases of minimum S/B: 0, 0.65, 1, 1.2 and 1.4. See Table 11.

The significances and S/B from Table 11 are directly obtained from Figure 16. With the several optimised selections for the different requirements of minimum S/B,

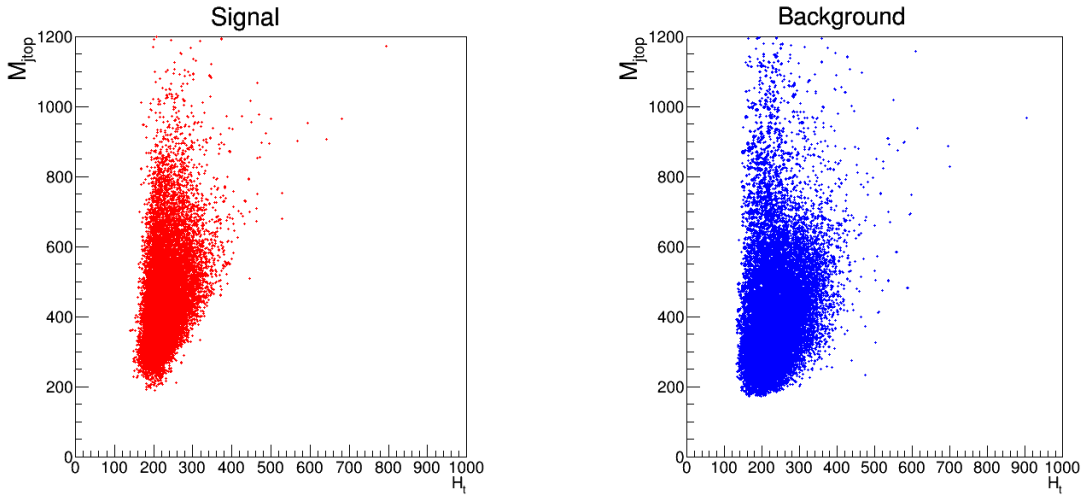

Figure 15: Correlation between H_T and $m_{j,top}$ for 13 TeV MC samples after the preselection, $m_{l,b}$, m_{top}, $\Delta\eta_{j,top}$ and $|\eta_j|$ requirements are applied. Electron channel. In this scatter two dimensional plot the signal has been scaled by a factor 0.1 and the background by a factor 0.05 for aesthetic purposes.

Min. S/B	Significance	S/B	$H_T(min)$	$m_{j,top}(min)$
0.00	81.9	0.598	168	284
0.65	81.0	0.654	176	316
1.00	63.5	1.006	192	512
1.20	51.9	1.202	212	608
1.40	37.3	1.406	192	824

Table 11: Significances and S/B ratios for 13 TeV MC samples depending on the cuts applied over $m_{j,top}$ and H_T for different cases of minimum S/B. The preselection, $m_{l,b}$, m_{top}, $\Delta\eta_{j,top}$ and $|\eta_j|$ requirements, are applied.

selection regions are defined and their event yields are shown in Table 12. There can be seen that the predictions of significance and S/B from Table 11 are in agreement with the calculations with the event yields of Table 12.

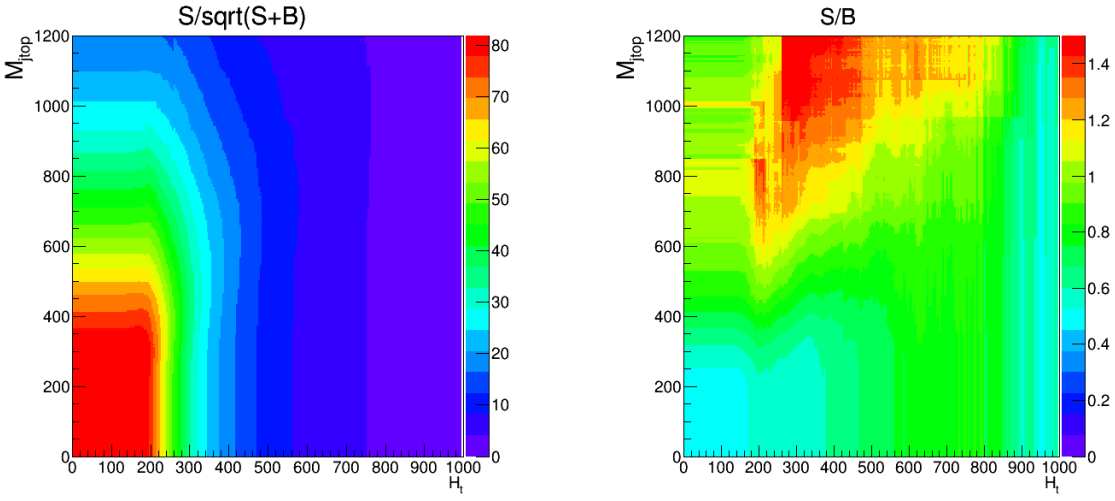

Figure 16: Maps of significance and S/B depending on the $H_T(min)$ and $m_{j,top}(min)$ used for the cuts. The preselection, $m_{l,b}$, m_{top}, $\Delta\eta_{j,top}$ and $|\eta_j|$ requirements, are also considered.

	Event yields. $(H_T(min), m_{j,top}(min))$				
Process	(168, 284)	(176, 316)	(192, 512)	(212, 608)	(192, 824)
t-channel	17929 ± 83	16604 ± 80	8043 ± 57	4943 ± 45	2376 ± 31
Z-jet, diboson	841 ± 85	658 ± 74	192 ± 49	50 ± 12	13 ± 10
W+jets	13189 ± 704	10996 ± 654	3267 ± 389	1532 ± 326	622 ± 314
$t\bar{t}$	12088 ± 74	10564 ± 69	3456 ± 40	1963 ± 30	729 ± 19
Wt s-channel	2052 ± 33	1684 ± 29	508 ± 16	277 ± 13	106 ± 7
Multijet	1795 ± 45	1472 ± 40	572 ± 26	290 ± 19	220 ± 18
Total	47895 ± 720	41979 ± 668	16038 ± 399	9056 ± 332	4065 ± 317
Significance	82	81	64	52	37
S/B	0.598	0.654	1.006	1.202	1.406

Table 12: Event yields for 13 TeV MC samples after applying the preselection requirements, $m_{l,b} < 140$ GeV, $142 < m_{top} < 418$ GeV, $|\eta_j| > 3.5 - \Delta\eta_{j,top}$ and $m_{j,top}$ and H_T cuts. Each columns refers to a different set of lower cuts in $m_{j,top}$ and H_T according to the optimisation of Table 11.

6 Conclusion

During this master thesis a comprehensive review of the theoretical framework and of the current status of the analyses that have explored the Wtb vertex using t-channel single-top-quark events produced at the LHC has been done. Specifically, a new optimised set of selection cuts has been defined for the t-channel production at $\sqrt{s}$=13 TeV in the ATLAS detector of LHC. The variables considered in this analysis provide a fairly good background discrimination and, at the same time, do not employ kinematic properties of a single or two top quark decay products. Hence, their choice try to avoid potential kinematic biases in the angular distributions used in the measurement of the polarisation observables sensitive to the anomalous couplings.

The whole optimisation criteria described in Section 5 leads to a proposal of the set of variables to be considered in the selection together with different values of the optimised cuts that correspond to different choices of the ratio S/B together with the statistical significance (see Table 12).

This work will benefit the Run II ATLAS analyses of the Wtb vertex using t-channel single-top-quark events, providing a baseline selection for the data sample to be used in these incoming analyses and ensuring an statistical optimisation. Further considerations will have to be taking into account when evaluating the systematic uncertainties at the end of the whole analysis chain.

A Correlations among the selection variables and the polarisation angles

In this appendix, the correlations between the six variables used in our final set of selection cuts (m_{top}, H_T, η_j, $\Delta\eta_{j,top}$, $m_{j,top}$ and $m_{l,b}$) and the angular distributions of the cosines of the angles (θ_l, LX, LY and θ_l^*) are shown. It is important that a cut on a variable does not remove signal events from the polarisation distributions, otherwise, that variable is not adequate to be included in the set of cuts. The displayed angles are those of Section 2, with the axis definition of reference [22]:

$\cos(\theta_l)$: Cosine of the top-quark polarisation in the $\hat{z}$-axis. The θ_l is the angle between the momentum of the charged lepton in the top-quark reference frame with the top-quark spin direction, $\hat{s}_t$. This direction $\hat{s}_t$ is calculated as the spectator jet momentum boosted to the top-quark reference frame. Figures 17-22.

$\cos(LX)$: Cosine of the top-quark polarisation in the $\hat{x}$-axis. The angle LX is the one formed by the charged lepton in the top-quark reference frame and the $\hat{x}$ defined in equation 7. Figures 23-28.

$\cos(LY)$: Cosine of the top-quark polarisation in the $\hat{y}$-axis. The angle LX is the one formed by the charged lepton in the top-quark reference frame and the $\hat{y}$ defined in equation 6. Figures 29-34.

$\cos(\theta_l^*)$: Cosine of the W-boson helicity. θ_l^* is the angle of the W-boson momentum in the top-quark reference frame and the charged lepton in the W-boson rest frame. Figures 35-39.

Figures 17-39 are generated at preselection level (Table 5).

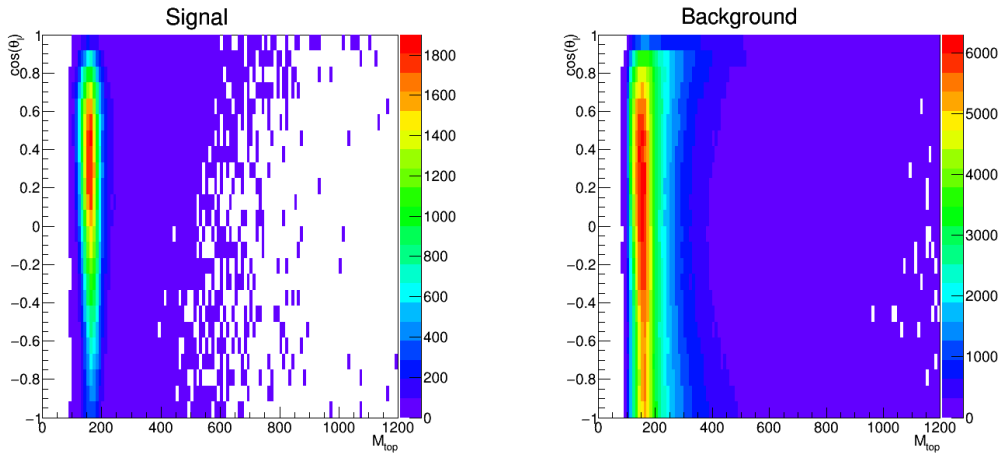

Figure 17: Two-dimensional distributions of $\cos(\theta_l)$ versus m_{top}.

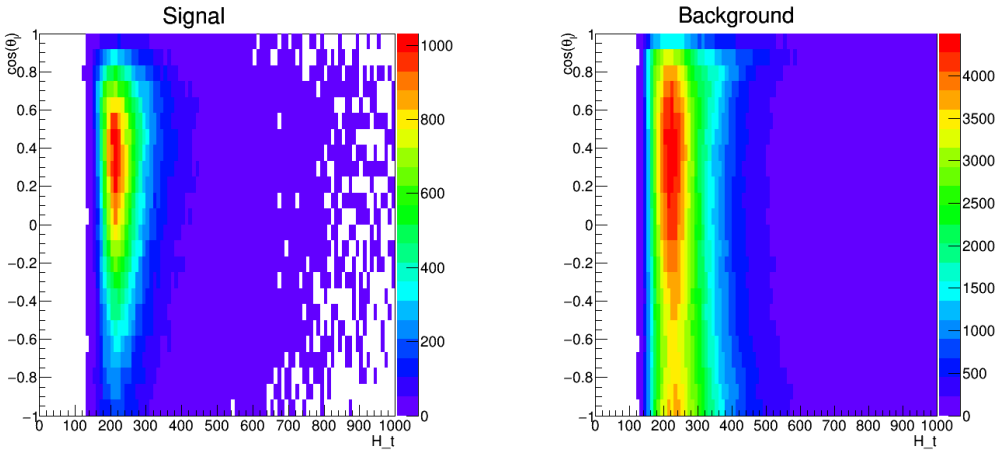

Figure 18: Two-dimensional distributions of $\cos(\theta_l)$ versus H_T.

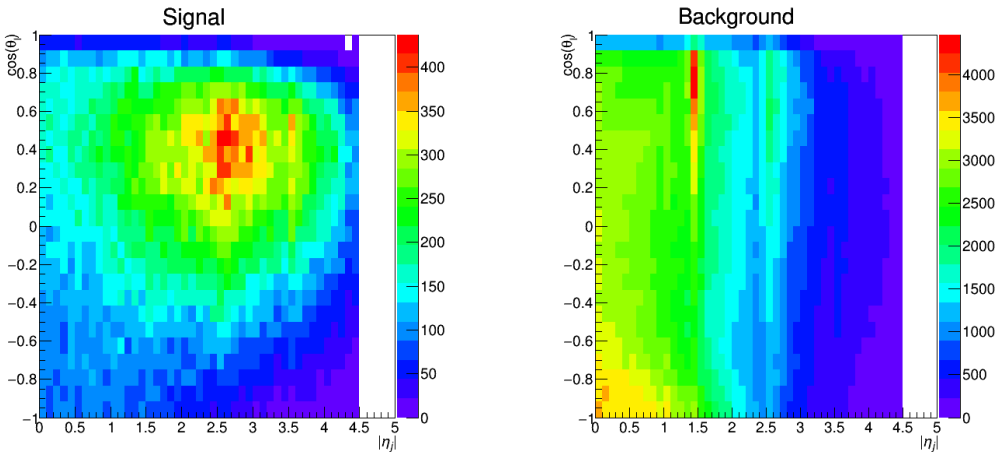

Figure 19: Two-dimensional distributions of $\cos(\theta_l)$ versus η_j.

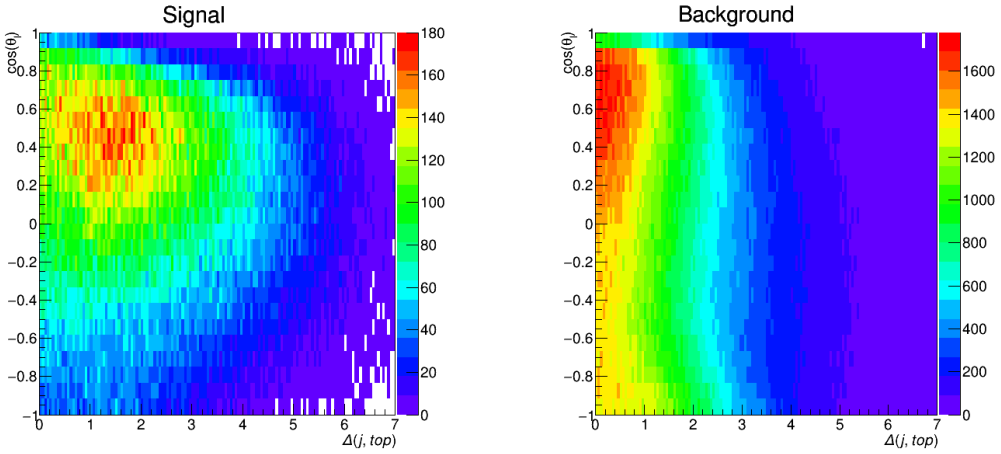

Figure 20: Two-dimensional distributions of $\cos(\theta_l)$ versus $\Delta\eta_{j,top}$.

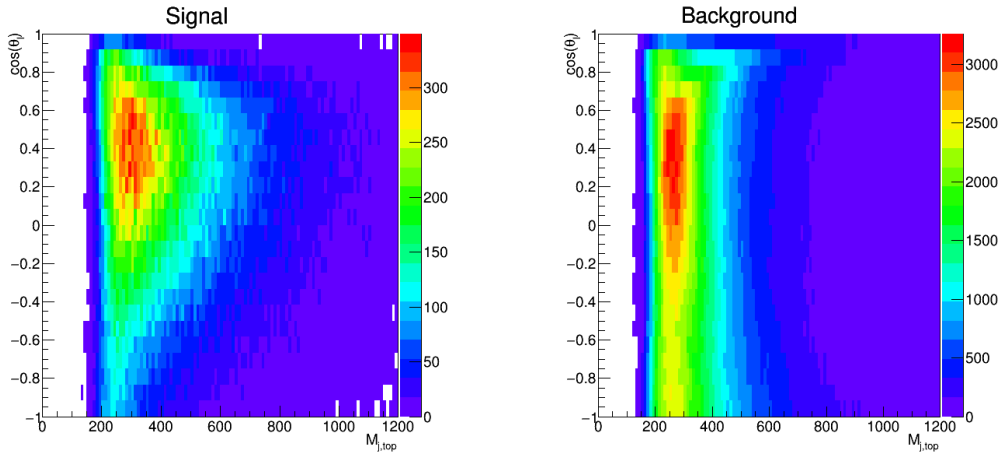

Figure 21: Two-dimensional distributions of $\cos(\theta_l)$ versus $m_{j,top}$.

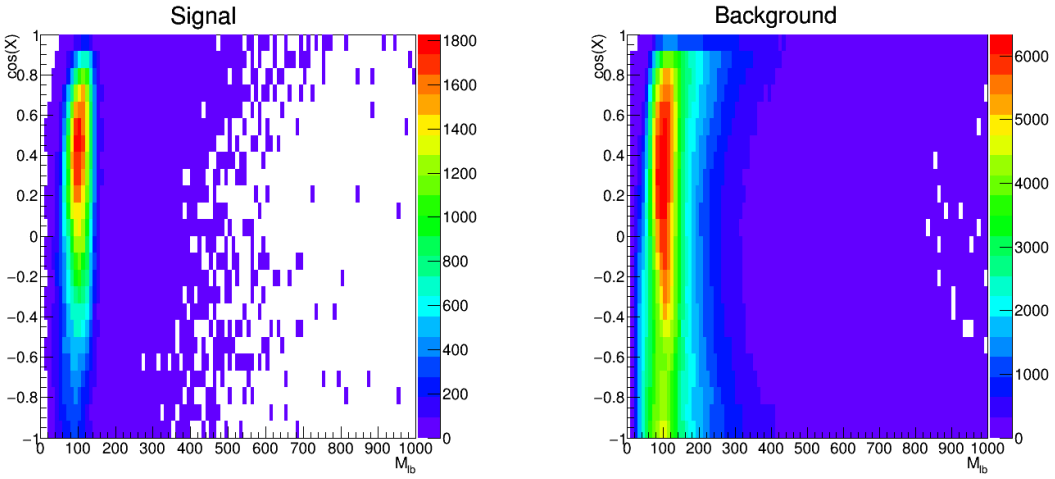

Figure 22: Two-dimensional distributions of $\cos(\theta_l)$ versus $m_{l,b}$.

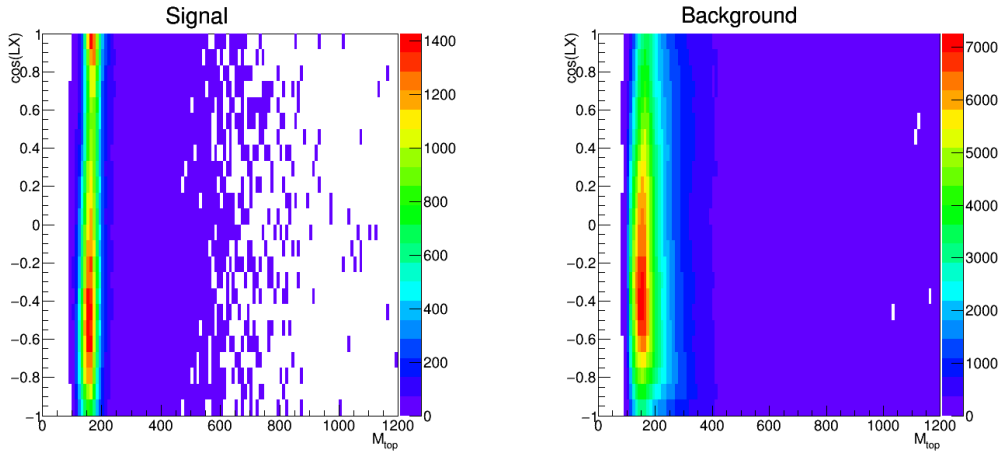

Figure 23: Two-dimensional distributions of $\cos(LX)$ versus m_{top}.

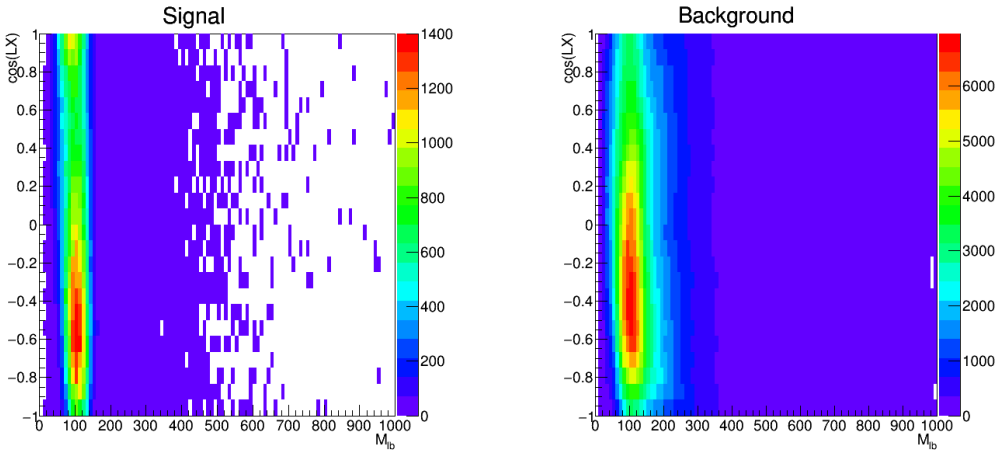

Figure 24: Two-dimensional distributions of $\cos(LX)$ versus H_T.

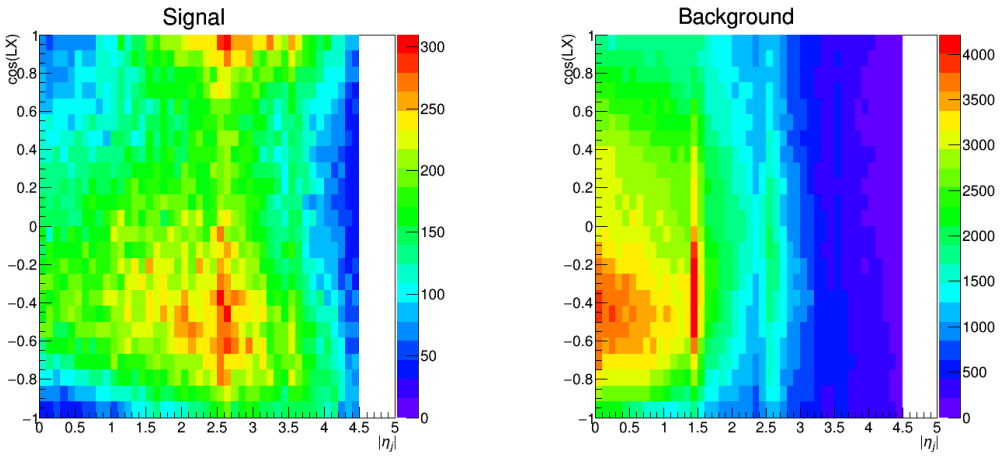

Figure 25: Two-dimensional distributions of $\cos(LX)$ versus η_j.

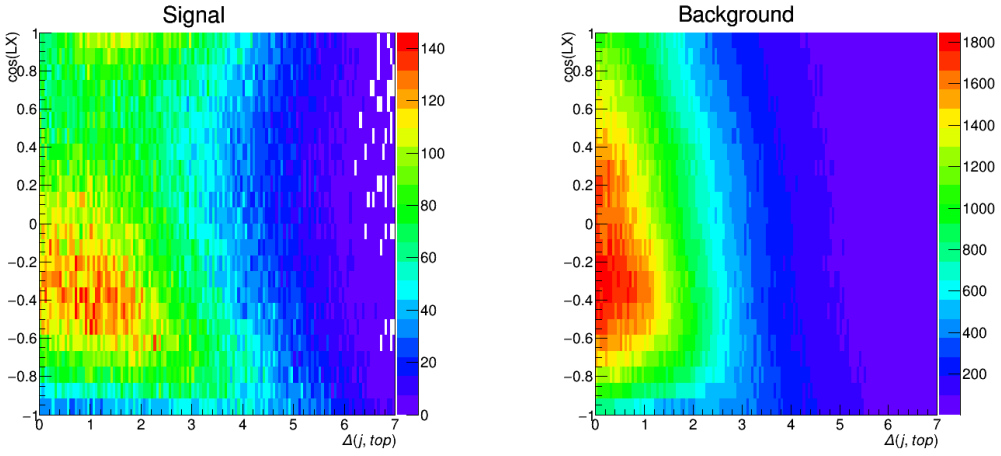

Figure 26: Two-dimensional distributions of $\cos(LX)$ versus $\Delta\eta_{j,top}$.

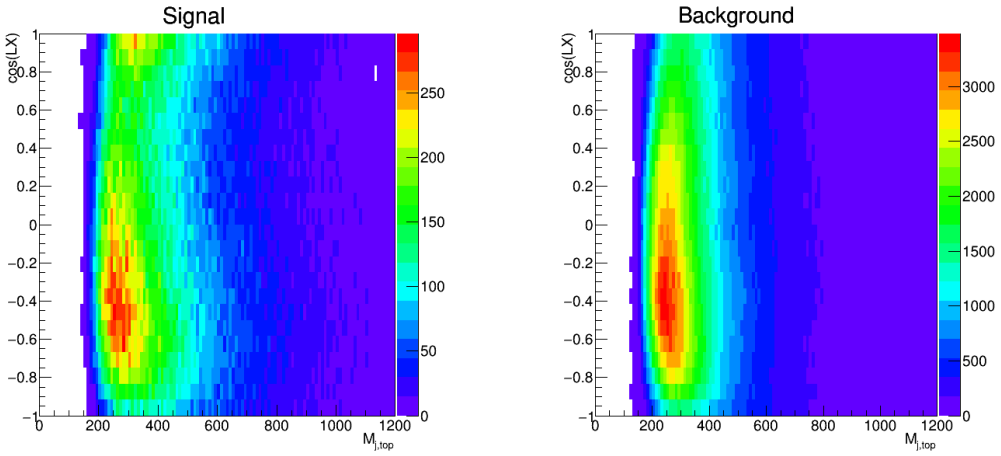

Figure 27: Two-dimensional distributions of $\cos(LX)$ versus $m_{j,top}$.

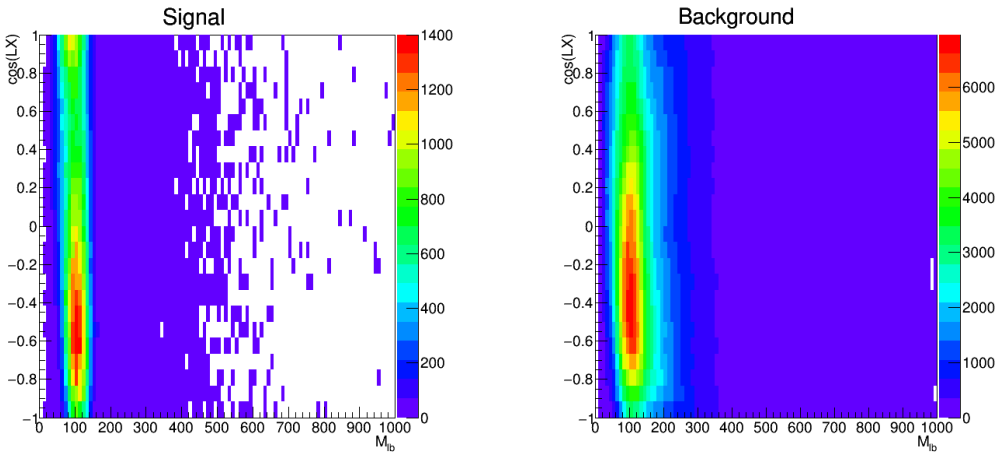

Figure 28: Two-dimensional distributions of $\cos(LX)$ versus $m_{l,b}$.

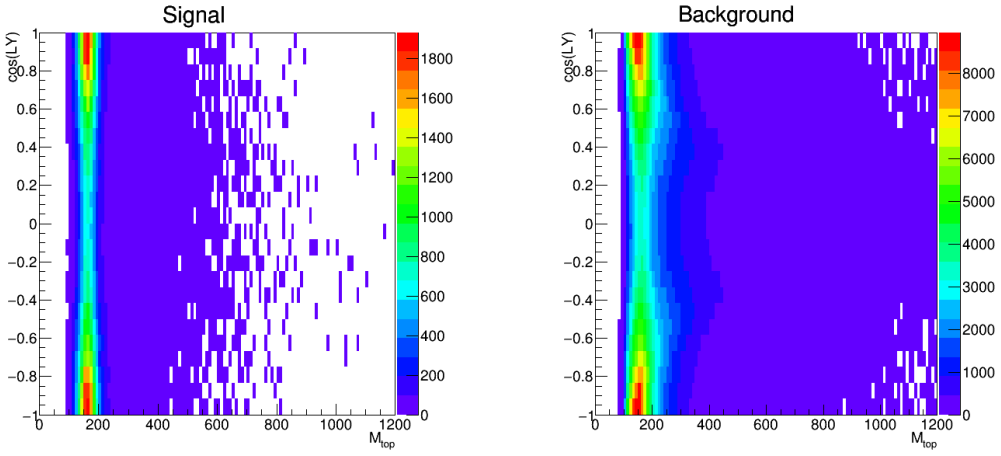

Figure 29: Two-dimensional distributions of $\cos(LY)$ versus m_{top}.

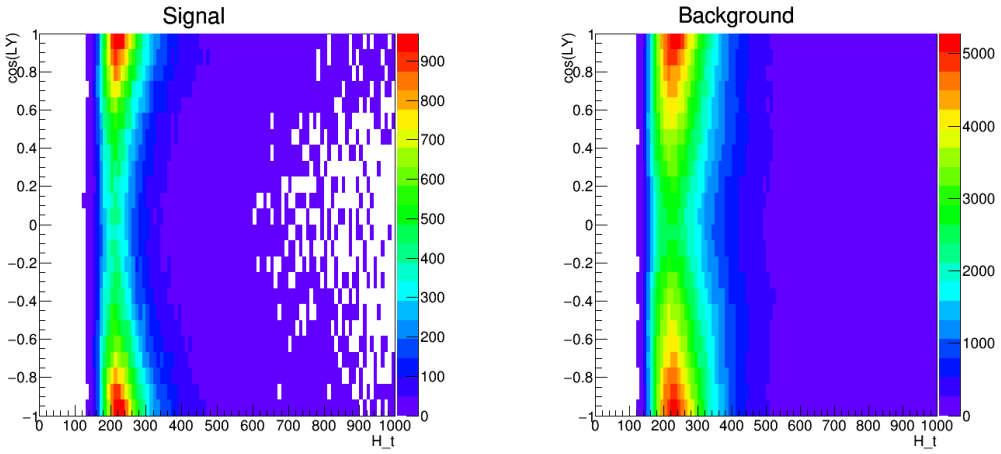

Figure 30: Two-dimensional distributions of $\cos(LY)$ versus H_T.

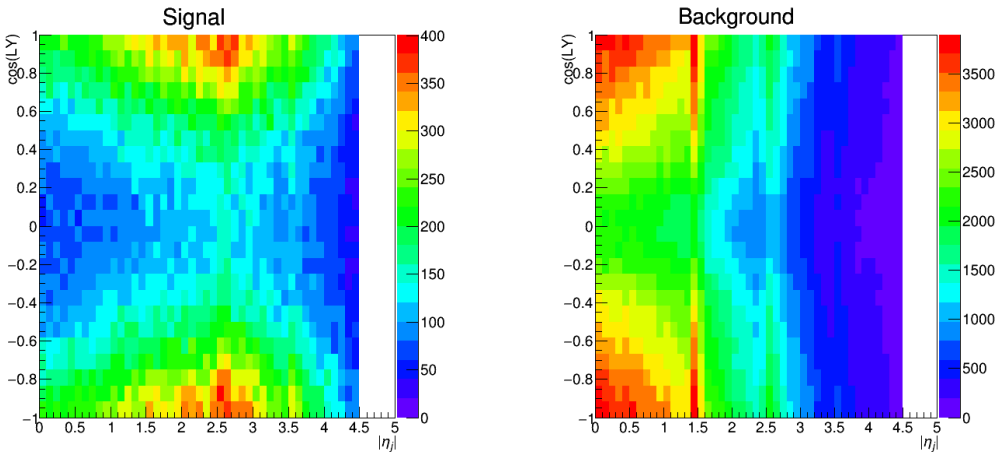

Figure 31: Two-dimensional distributions of $\cos(LY)$ versus η_j.

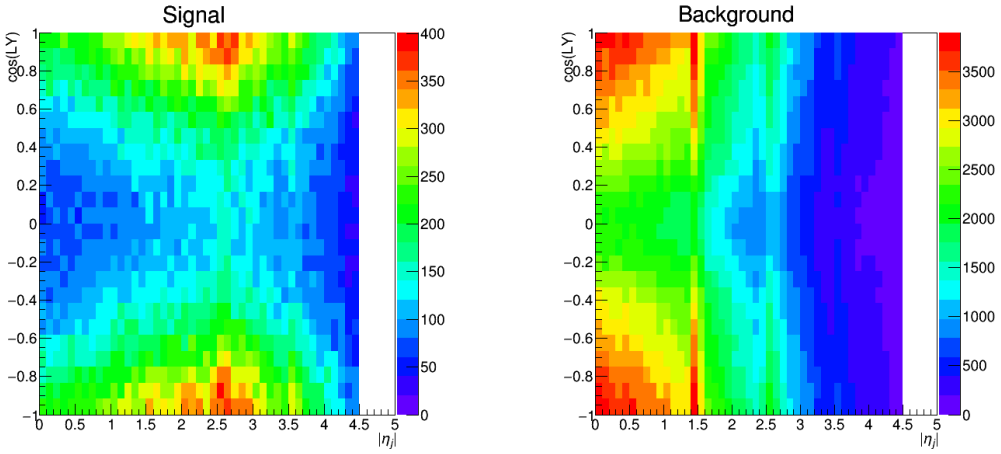

Figure 32: Two-dimensional distributions of $\cos(LY)$ versus $\Delta\eta_{j,top}$.

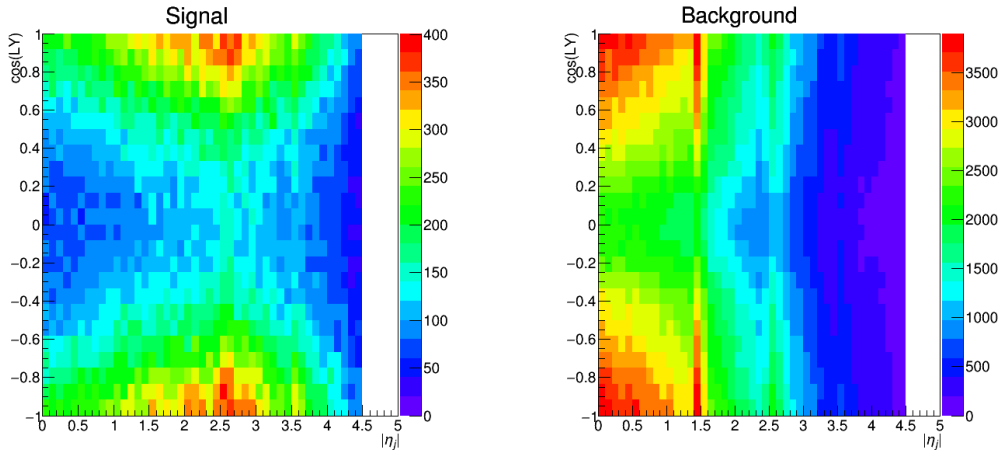

Figure 33: Two-dimensional distributions of $\cos(LY)$ versus $m_{j,top}$.

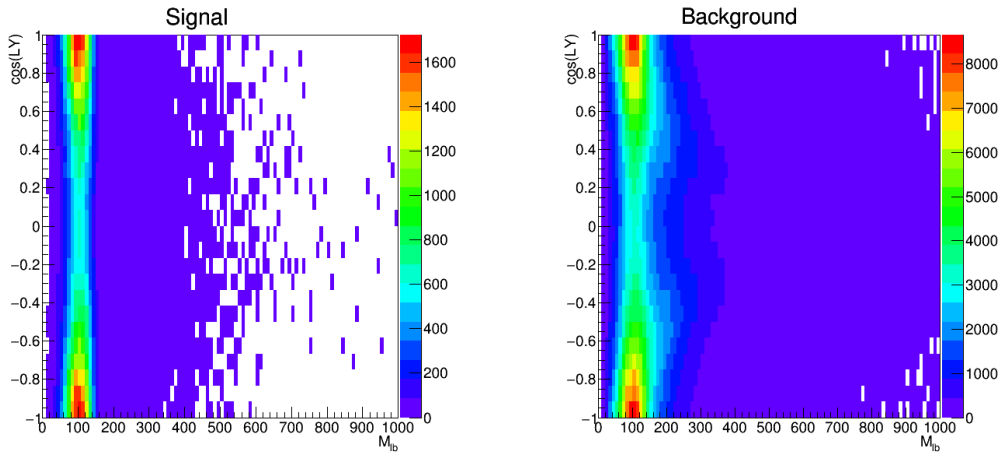

Figure 34: Two-dimensional distributions of $\cos(LY)$ versus $m_{l,b}$.

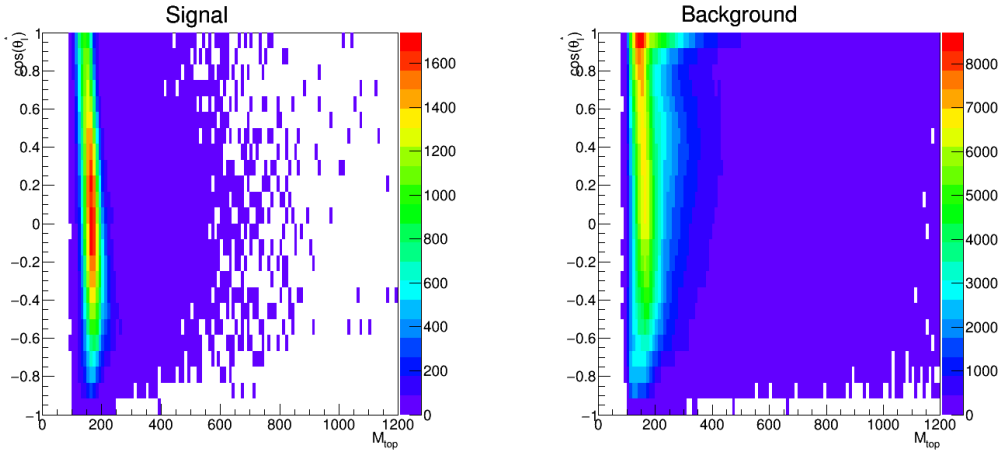

Figure 35: Two-dimensional distributions of $\cos(\theta_l^*)$ versus m_{top}.

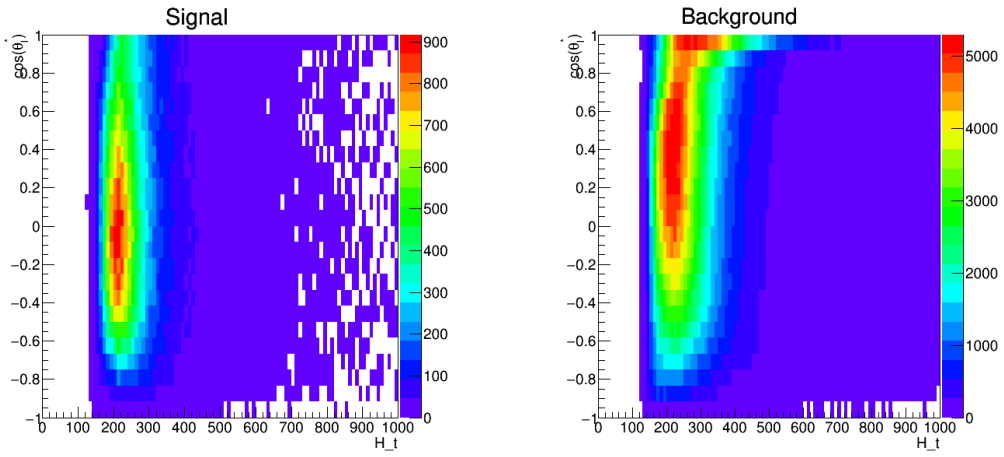

Figure 36: Two-dimensional distributions of $\cos(\theta_l^*)$ versus H_T.

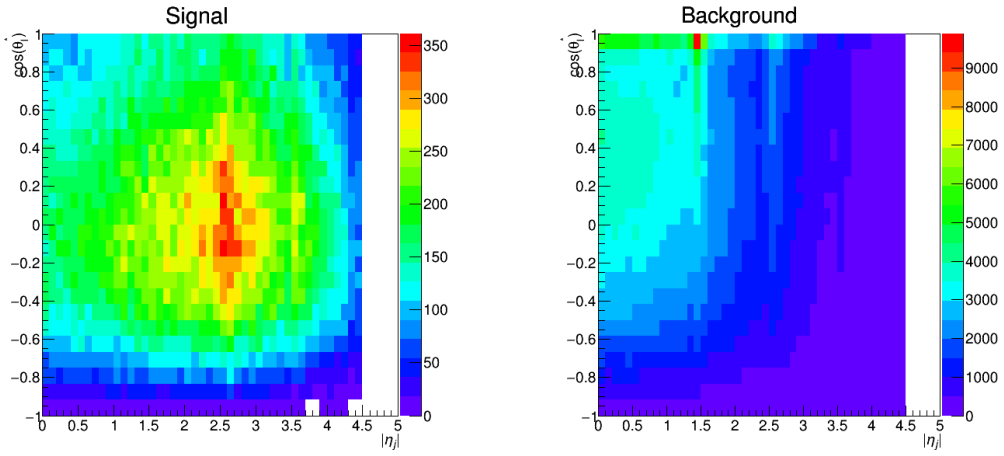

Figure 37: Two-dimensional distributions of $\cos(\theta_l^*)$ versus η_j.

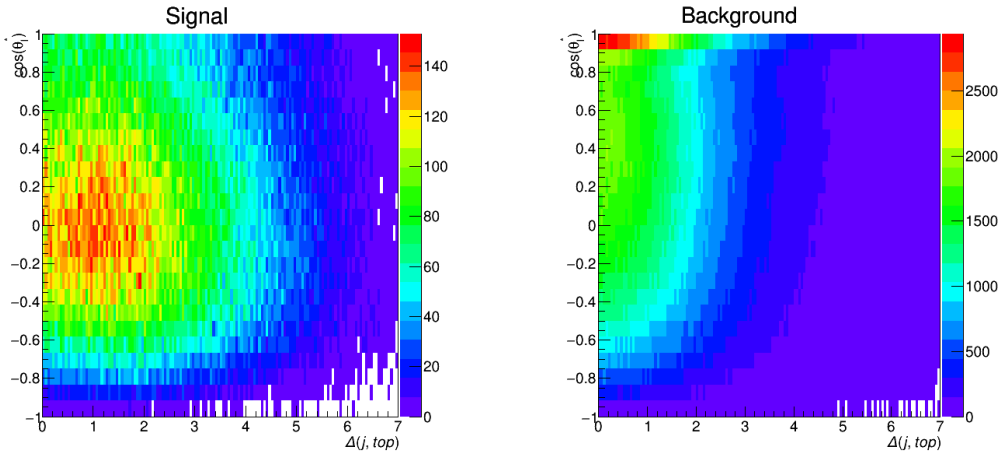

Figure 38: Two-dimensional distributions of $\cos(\theta_l^*)$ versus $\Delta\eta_{j,top}$.

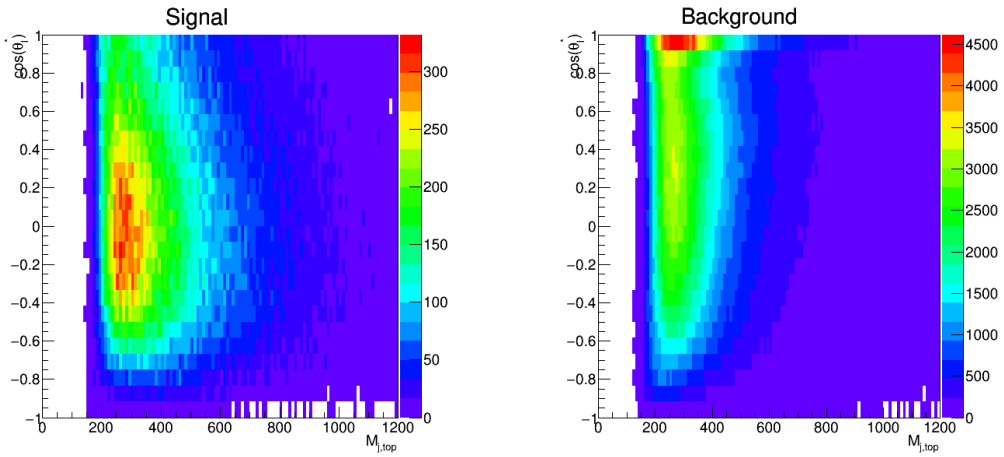

Figure 39: Two-dimensional distributions of $\cos(\theta_l^*)$ versus $m_{j,top}$.

References

[1] R. Oerter, *The theory of almost everything: The standard model, the unsung triumph of modern physics*. Penguin, 2006.

[2] L. Canetti, M. Drewes, and M. Shaposhnikov, *Matter and Antimatter in the Universe*, New J. Phys. **14** (2012) 095012, arXiv:1204.4186 [hep-ph].

[3] J. H. Christenson, J. W. Cronin, V. L. Fitch, and R. Turlay, *Evidence for the* 2π *Decay of the* K_2^0 *Meson*, Phys. Rev. Lett. **13** (1964) 138–140.

[4] G. Mahlon and S. J. Parke, *Improved spin basis for angular correlation studies in single top quark production at the Tevatron*, Phys. Rev. **D55** (1997) 7249–7254, arXiv:hep-ph/9611367.

[5] CMS Collaboration, *Measurement of the top quark mass using proton-proton data at* $\sqrt{s}$ *= 7 and 8 TeV*, Phys. Rev. **D93** (2016) 072004, arXiv:1509.04044 [hep-ex].

[6] ATLAS and CMS Collaborations, *Combined Measurement of the Higgs Boson Mass in pp Collisions at* $\sqrt{s} = 7$ *and 8 TeV with the ATLAS and CMS Experiments*, Phys. Rev. Lett. **114** (2015) 191803, arXiv:1503.07589 [hep-ex].

[7] Particle Data Group Collaboration, *Review of Particle Physics*, Chin. Phys. **C40** (2016) 100001.

[8] M. Kobayashi and T. Maskawa, *CP Violation in the Renormalizable Theory of Weak Interaction*, Prog. Theor. Phys. **49** (1973) 652–657.

[9] D0 Collaboration, *Observation of Top Quark Production in* $\overline{p}p$ *Collisions with the Collider Detector at Fermilab*, Phys. Rev. Lett. **74** (1995) 2626–2631.

[10] D0 Collaboration, *Observation of the top quark*, Phys. Rev. Lett. **74** (1995) 2632–2637, arXiv:hep-ex/9503003 [hep-ex].

[11] Nobelprize.org, *The Nobel Prize in Physics*, 2008. https://www.nobelprize.org/nobel_prizes/physics/laureates/2008/.

[12] I. I. Y. Bigi, Y. L. Dokshitzer, V. A. Khoze, J. H. Kuhn, and P. M. Zerwas, *Production and Decay Properties of Ultraheavy Quarks*, Phys. Lett. **B181** (1986) 157–163.

[13] ATLAS Collaboration, *Probing the Wtb vertex structure in t-channel single-top-quark production and decay in pp collisions at* $\sqrt{s} = 8$ *TeV with the ATLAS detector*, JHEP **04** (2017) 124, arXiv:1702.08309 [hep-ex].

[14] D. Hirschbuehl, *Single-top quark cross-section measurements in ATLAS*, in *Proceedings, 9th International Workshop on Top Quark Physics (TOP 2016): Olomouc, Czech Republic, September 19-23, 2016*. 2017. arXiv:1703.02360 [hep-ex].

[15] ATLAS Collaboration, *Measurement of the inclusive cross-sections of single top-quark and top-antiquark t-channel production in pp collisions at $\sqrt{s}$ = 13 TeV with the ATLAS detector*, JHEP **04** (2017) 086, arXiv:1609.03920 [hep-ex].

[16] N. Kidonakis, *Next-to-next-to-leading-order collinear and soft gluon corrections for t-channel single top quark production*, Phys. Rev. **D83** (2011) 091503, arXiv:1103.2792 [hep-ph].

[17] N. Kidonakis, *Two-loop soft anomalous dimensions for single top quark associated production with a W- or H-*, Phys. Rev. **D82** (2010) 054018, arXiv:1005.4451 [hep-ph].

[18] N. Kidonakis, *NNLL resummation for s-channel single top quark production*, Phys. Rev. **D81** (2010) 054028, arXiv:1001.5034 [hep-ph].

[19] P. Kant, O. M. Kind, T. Kintscher, T. Lohse, T. Martini, S. Mölbitz, P. Rieck, and P. Uwer, *HatHor for single top-quark production: Updated predictions and uncertainty estimates for single top-quark production in hadronic collisions*, Comput. Phys. Commun. **191** (2015) 74–89, arXiv:1406.4403 [hep-ph].

[20] M. Aliev, H. Lacker, U. Langenfeld, S. Moch, P. Uwer, and M. Wiedermann, *HATHOR: HAdronic Top and Heavy quarks crOss section calculatoR*, Comput. Phys. Commun. **182** (2011) 1034–1046, arXiv:1007.1327 [hep-ph].

[21] J. A. Aguilar-Saavedra and J. Bernabeu, *W polarisation beyond helicity fractions in top quark decays*, Nucl. Phys. **B840** (2010) 349–378, arXiv:1005.5382 [hep-ph].

[22] J. A. Aguilar-Saavedra and S. Amor Dos Santos, *New directions for top quark polarization in the t-channel process*, Phys. Rev. **D89** (2014) 114009, arXiv:1404.1585 [hep-ph].

[23] ATLAS Collaboration, *Measurement of the W boson polarisation in $t\bar{t}$ events from pp collisions at $\sqrt{s}$ = 8 TeV in the lepton + jets channel with ATLAS*, Eur. Phys. J. **C77** (2017) 264, arXiv:1612.02577 [hep-ex].

[24] ATLAS Collaboration, *Analysis of the Wtb vertex from the measurement of triple-differential angular decay rates of single top quarks produced in the t-channel at $\sqrt{s}$ = 8 TeV with the ATLAS detector*, arXiv:1707.05393 [hep-ex].

[25] CMS Collaboration, *Search for anomalous Wtb couplings and flavour-changing neutral currents in t-channel single top quark production in pp collisions at $\sqrt{s}$ = 7 and 8 TeV*, JHEP **02** (2017) 028, arXiv:1610.03545 [hep-ex].

[26] M. Komm, *Measurement of Top-Quark Polarization in t-channel Single-Top Production*, in *Proceedings, 7th International Workshop on Top Quark Physics (TOP2014): Cannes, France, September 28-October 3, 2014*. 2014. arXiv:1412.0106 [hep-ex].

[27] CMS Collaboration, *Measurement of top quark polarization in t-channel single-top production*, 2013, https://cds.cern.ch/record/1601800.

[28] J. A. Aguilar-Saavedra, *Single top quark production at LHC with anomalous Wtb couplings*, Nucl. Phys. **B804** (2008) 160–192, arXiv:0803.3810 [hep-ph].

[29] P. M. Nadolsky, H.-L. Lai, Q.-H. Cao, J. Huston, J. Pumplin, D. Stump, W.-K. Tung, and C. P. Yuan, *Implications of CTEQ global analysis for collider observables*, Phys. Rev. **D78** (2008) 013004, arXiv:0802.0007 [hep-ph].

[30] R. Schwienhorst, C. P. Yuan, C. Mueller, and Q.-H. Cao, *Single top quark production and decay in the t-channel at next-to-leading order at the LHC*, Phys. Rev. **D83** (2011) 034019, arXiv:1012.5132 [hep-ph].

[31] J. M. Campbell, R. Frederix, F. Maltoni, and F. Tramontano, *Next-to-Leading-Order Predictions for t-Channel Single-Top Production at Hadron Colliders*, Phys. Rev. Lett. **102** (2009) 182003, arXiv:0903.0005 [hep-ph].

[32] A. Brandenburg, Z. G. Si, and P. Uwer, *QCD corrected spin analyzing power of jets in decays of polarized top quarks*, Phys. Lett. **B539** (2002) 235–241, arXiv:hep-ph/0205023.

[33] CMS Collaboration, *Measurement of top quark polarisation in t-channel single top quark production*, JHEP **04** (2016) 073, arXiv:1511.02138 [hep-ex].

[34] J. A. Aguilar-Saavedra and J. Bernabeu, *Breaking down the entire W boson spin observables from its decay*, Phys. Rev. **D93** (2016) 011301, arXiv:1508.04592 [hep-ph].

[35] A. Czarnecki, J. G. Korner, and J. H. Piclum, *Helicity fractions of W bosons from top quark decays at NNLO in QCD*, Phys. Rev. **D81** (2010) 111503, arXiv:1005.2625 [hep-ph].

[36] Gargamelle Neutrino Collaboration, *Observation of Neutrino Like Interactions Without Muon Or Electron in the Gargamelle Neutrino Experiment*, Phys. Lett. **46B** (1973) 138–140.

[37] P. M. Watkins, *Discovery of the W and Z bosons*, Contemp. Phys. **27** (1986) 291–324.

[38] ALEPH Collaboration, *Determination of the number of light neutrino species*, Phys. Lett. **B231** (1989) 519–529.

[39] NA48 Collaboration, *A New measurement of direct CP violation in two pion decays of the neutral kaon*, Phys. Lett. **B465** (1999) 335–348, arXiv:hep-ex/9909022 [hep-ex].

[40] D. Carmi, A. Falkowski, E. Kuflik, T. Volansky, and J. Zupan, *Higgs After the Discovery: A Status Report*, JHEP **10** (2012) 196, arXiv:1207.1718 [hep-ph].

[41] L. Evans and P. Bryant, *LHC Machine*, JINST **3** (2008) S08001.

[42] S. Myers, *The LEP collider, from design to approval and commissioning*, CERN-91-08, CERN-YELLOW-91-08. 1991.

[43] B. Muller, J. Schukraft, and B. Wyslouch, *First Results from Pb+Pb collisions at the LHC*, Ann. Rev. Nucl. Part. Sci. **62** (2012) 361–386, arXiv:1202.3233 [hep-ex].

[44] CMS Collaboration, *The CMS Experiment at the CERN LHC*, JINST **3** (2008) S08004.

[45] ALICE Collaboration, *The ALICE experiment at the CERN LHC*, JINST **3** (2008) S08002.

[46] LHCb Collaboration, *The LHCb Detector at the LHC*, JINST **3** (2008) S08005.

[47] TOTEM Collaboration, *The TOTEM experiment at the CERN Large Hadron Collider*, JINST **3** (2008) S08007.

[48] LHCf Collaboration, *The LHCf detector at the CERN Large Hadron Collider*, JINST **3** (2008) S08006.

[49] MoEDAL Collaboration, *Technical design report of the MoEDAL experiment*, 2009, https://cds.cern.ch/record/1181486.

[50] A. Hoecker, *Physics at the LHC Run-2 and Beyond*, in *2016 European School of High-Energy Physics (ESHEP 2016) Skeikampen, Norway, June 15-28, 2016*. 2016. arXiv:1611.07864 [hep-ex].

[51] R. Bruce, G. Arduini, H. Bartosik, R. De Maria, M. Giovannozzi, G. Iadarola, J. Jowett, K. S. B. Li, M. Lamont, A. Lechner, E. Metral, D. Mirarchi, T. Pieloni, S. Redaelli, G. Rumolo, B. Salvant, R. Tomas Garcia, and J. Wenninger, *LHC Run 2: Results and Challenges*, 2016, https://cds.cern.ch/record/2201447.

[52] ATLAS Collaboration, "Luminosity public results.". https://twiki.cern.ch/twiki/bin/view/AtlasPublic/LuminosityPublicResultsRun2.

[53] ATLAS Collaboration, *ATLAS: Detector and physics performance technical design report. Volume 1*, 1999, https://cds.cern.ch/record/391176.

[54] M. E. Pozo Astigarraga, *Evolution of the ATLAS Trigger and Data Acquisition System*, J. Phys. Conf. Ser. **608** (2015) 012006.

[55] ATLAS Collaboration, *The ATLAS Simulation Infrastructure*, Eur. Phys. J. **C70** (2010) 823–874, arXiv:1005.4568 [physics.ins-det].

[56] GEANT4 Collaboration, *GEANT4: A Simulation toolkit*, Nucl. Instrum. Meth. **A506** (2003) 250–303.

[57] M. Moreno Llácer, *Search for CP violation in single top quark events with the ATLAS detector at LHC*. PhD thesis, University of Valencia, IFIC, 2014. https://inspirehep.net/record/1339903/files/CERN-THESIS-2014-070.pdf.

[58] S. Alioli, P. Nason, C. Oleari, and E. Re, *A general framework for implementing NLO calculations in shower Monte Carlo programs: the POWHEG BOX*, JHEP **2010** (2010) 43.

[59] T. Sjostrand, S. Mrenna, and P. Z. Skands, *PYTHIA 6.4 Physics and Manual*, JHEP **05** (2006) 026, arXiv:hep-ph/0603175.

[60] T. Gleisberg, S. Höche, F. Krauss, M. Schönherr, S. Schumann, F. Siegert, and J. Winter, *Event generation with SHERPA 1.1*, JHEP **02** (2009) 007, arXiv:0811.4622 [hep-ph].

[61] ATLAS Collaboration, *Estimation of non-prompt and fake lepton backgrounds in final states with top quarks produced in proton-proton collisions at* $\sqrt{s} = 8$ *TeV with the ATLAS detector*, 2014, https://cds.cern.ch/record/1951336.

[62] ATLAS Collaboration, *Electron reconstruction and identification efficiency measurements with the ATLAS detector using the 2011 LHC proton-proton collision data*, Eur. Phys. J. **C74** (2014) 2941, arXiv:1404.2240 [hep-ex].

[63] ATLAS Collaboration, *Electron efficiency measurements with the ATLAS detector using the 2012 LHC proton-proton collision data*, 2014, https://cds.cern.ch/record/1706245.

[64] ATLAS Collaboration, *Measurement of the* $t\bar{t}$ *production cross-section using* $e\mu$ *events with b-tagged jets in pp collisions at* $\sqrt{s}$*=13 TeV with the ATLAS detector*, Phys. Lett. **B761** (2016) 136–157, arXiv:1606.02699 [hep-ex].

[65] M. Cacciari, G. P. Salam, and G. Soyez, *The Anti-k(t) jet clustering algorithm*, JHEP **04** (2008) 063, arXiv:0802.1189 [hep-ph].

[66] ATLAS Collaboration, *Monte Carlo Calibration and Combination of In-situ Measurements of Jet Energy Scale, Jet Energy Resolution and Jet Mass in ATLAS*, 2015, https://cds.cern.ch/record/2044941.

[67] ATLAS Collaboration, *Performance of pile-up mitigation techniques for jets in pp collisions at* $\sqrt{s} = 8$ *TeV using the ATLAS detector*, Eur. Phys. J. **C76** (2016) 581, arXiv:1510.03823 [hep-ex].

[68] ATLAS Collaboration, *Performance of the ATLAS muon trigger in pp collisions at* $\sqrt{s} = 8$ *TeV*, Eur. Phys. J. **C75** (2015) 120, arXiv:1408.3179 [hep-ex].

[69] ATLAS Collaboration, *Comprehensive measurements of t-channel single top-quark production cross sections at* $\sqrt{s} = 7$ *TeV with the ATLAS detector*, Phys. Rev. **D90** no. 11, (2014) 112006, arXiv:1406.7844 [hep-ex].

[70] G. Punzi, *Sensitivity of searches for new signals and its optimization*, eConf **C030908** (2003) MODT002, arXiv:physics/0308063.

[71] S. Pedraza-López, *Measurement of top quark and W boson polarization observables with t-channel single-top-quark events in the ATLAS experiment*. PhD thesis, University of Valencia, 2017.

[72] ATLAS Collaboration, *Fiducial, total and differential cross-section measurements of t-channel single top-quark production in pp collisions at 8 TeV using data collected by the ATLAS detector*, Eur. Phys. J. **C77** (2017) 531, arXiv:1702.02859 [hep-ex].